Assessing the Effect of Topography on Cs-137 Concentrations within Forested Soils due to the Fukushima Daiichi Nuclear Power Plant Accident, Japan

Misa Yasumiishi[1], Taku Nishimura[2], Jared Aldstadt[1], Sean J. Bennett[1], Thomas Bittner[1]

[1]Department of Geography, State University of New York, the University at Buffalo

[2]Laboratory of Soil Physics and Soil Hydrology, Graduate School of Agricultural and Life Sciences, The University of Tokyo

Correspondence to: Misa Yasumiishi (misayasu@buffalo.edu)

Abstract. Topographic effects on Cs-137 concentrations in a forested area were quantitatively examined using 58 soil core samples collected in a village in Fukushima, Japan, which was directly impacted by the radioactive plume emitted during the 2011 Fukushima Daiichi Nuclear Power Plant (FDNPP) accident. In this study, five topographic parameters and two soil properties were evaluated as controls on the soil Cs-137 concentration using generalized additive models (GAM), a flexible statistical method for evaluating the functional dependencies of multiple parameters. GAMs employing soil dry bulk density, mass water content, and elevation explained 54% of the observed concentrations of Cs-137 within this landscape, whereas GAMs employing elevation, slope, and upslope distance explained 47% of the observed concentrations, which provide strong evidence of topographic effects on Cs-137 concentrations in soils. The model fit analysis confirmed that the topographic effects are strongest when multiple topographic parameters and soil properties are included. The ability of each topographic feature to predict Cs-137 concentrations was influenced by the resolution of the Digital Elevation Models. The movement of Cs-137 into the subsurface in this area near Fukushima was faster in comparison to regions affected by the Chernobyl Nuclear Power Plant accident. These results suggest that the effects of topographic parameters should be considered carefully in the use of anthropogenic radionuclides as environmental tracers and in the assessment of current and future environmental risks due to nuclear power plant accidents.

1. Introduction

On March 11, 2011, a 9.0 magnitude earthquake occurred near the northeast coast of Honshu, the largest island of Japan. A tsunami formed, arriving at the Fukushima Daiichi Nuclear Power Plant (FDNPP) approximately one hour later. A subsequent power outage caused the water circulation pumps to fail. This then led to overheating of the water, meltdowns, and hydrogen explosions (IAEA, 2015, Mahaffey, 2014). Nearby towns, villages, and farmlands were contaminated by the atmospheric fallout from the radioactive plume. Because human and environmental exposure to levels of elevated radiation can cause adverse health effects (EPA, 2017, Wrixon, 2004), the Japanese government designated an area within a 20 km radius of the FDNPP to be evacuated the next day.

One of the radionuclides released to the atmosphere during the accident was Cesium-137 (Cs-137). Cs-137 is an isotope of $_{55}$Cs, which emits gamma-rays with a half-life of 30.17 years (US EPA, 2017). Because of its long half-life, Cs-137 concentration in the environment is still a concern in Japan. Many studies have been conducted in the Fukushima region since the accident to assess the radioactivity of the land surface and environs (Table 1). Those studies confirmed that the majority of FDNPP-derived Cs-137 was concentrated in the soils close to the ground surface and exponentially decreased with depth, and that Cs-137's subsurface migration speed varied according to land use, soil types, and soil chemistry. Few studies, however, examined how local topography would affect Cs-137 concentrations accumulated by atmospheric fallout or subsequent remobilization on the land surface.

While Cs-137 is a byproduct of the nuclear energy generation process and does not exist in the environment naturally (Amaral, et al., 1998, IAEA, 2015, Tsoulfanidis, 2012), it has been used since the 1960s as an environmental tracer to understand surface soil and sediment movement (Walling and He, 1997). There are two primary pathways for Cs-137 once it is released in the environment. Cs-137 lacks a single valence electron and it is positively charged, which enables it to form electrovalent bonds with organic matter and mineral anions. Once Cs-137 is deposited on the ground, it becomes adsorbed to clay minerals (Claverie, et al., 2019, Fan, et al., 2014, Murota, et al., 2016, Nagao, 2016, Nakao, et al., 2008, Ohnuki and Kozai, 2013, Park, et al., 2019, Ritchie and Ritchie, 1995). It is this adsorption process that makes Cs-137 an effective environmental tracer for modeling surface soil loss, reservoir sedimentation, and sediment yield (Bennett, et al., 2005, Loughran, et al., 1987, Lowrance, et al., 1988, Mabit, et al., 2007, Martz and De Jong, 1987, Pennock, et al., 1995, Quine, et al., 1997, Ritchie and Ritchie, 1995, Wallbrink, et al., 2002, Walling, et al., 2007, Xinbao, et al., 1990). Water also provides an environmental pathway for Cs-137 transport; Cs-137 has a high water solubility and it can attach to sediment within surface waters (Iwagami, et al., 2015, Osawa, et al., 2018, Sakuma, et al., 2018, Tsuji, et al., 2016).

Topographic indices such as elevation and slope should play an important role in determining Cs-137 movement in the environment because these indices affect sediment transport and hydrologic processes (Catani, et al., 2010, Chen, et al., 1997, Griffiths, et al., 2009, Hoover and Hursh, 1943, Roering, et al., 2001, Roering, 2008, Roering, et al., 1999, Rossi, et al., 2014, Yang, et al., 1998). For example, Zaslavsky and Sinai (1981) noted that surface concavity was the controlling factor in distributing soil water in a catchment. Heimsath, et al., (1999) examined the relationships among cosmogenic nuclides, topographic curvature, and soil depth, and concluded that the variable thickness of soil is a function of topographic curvature. Studies using Cs-137 as a tracer found that topography affects runoff and infiltration and, hence, the concentration of Cs-137 in soils (Komissarov and Ogura, 2017, Martin-Garin, et al., 2012, Ritchie and McHenry, 1990, Walling, et al., 1995).

Cs-137 accumulation patterns in the Fukushima region can be compared to the Eastern European region affected by the Chernobyl Nuclear Power Plant (CNPP) accident in 1986. The CNPP and the FDNPP accidents are the only nuclear power plant accidents categorized as Level 7, which is the highest level on the International Nuclear and Radiological Event Scale (INES; IAEA, 2015, IAEA and INES, 2008, Mahaffey, 2014). The climate and topography of the Fukushima and Chernobyl regions differ (Table 2), and researchers suspect that Cs-137 concentrations on the landscape reflect these differences.

The overall goal of the research presented here is to understand the role of topography in determining the concentrations and distributions of Cs-137 on a landscape affected by the FDNPP accident. The objectives of the current study are as follows: (1) to define the concentrations and distributions of Cs-137 in surface and near-surface soil samples in a forested landscape directly impacted by the FDNPP accident, and (2) to quantitatively assess the control of topographic indices and soil properties on Cs-137 concentrations in this forested landscape using predictive analytics. It is envisioned that the primary data collected will contribute toward advancing the knowledge and understanding of the environmental hazards associated with radioactive fallout, societal response, and remediation actions, as well as elucidate the movement and long-term persistence of radionuclides in terrestrial environments.

2. Methods

2.1. Study Site Topography and Forests

Soil samples were collected in Iitate Village, a forested region located 35 km northwest of the FDNPP (Fig. 1). The study site was under the plume released on March 15, 2011. The plume initially moved toward the southwest and then, following a change in wind direction, toward the northwest, resulting in wet deposition across northwestern Fukushima and other prefectures (IAEA, 2015; Fig. 2). The Fukushima region is underlain by Paleozoic metamorphic rocks and Paleo-Mesozoic igneous rocks (Forest Management Center, 2017). The topography is composed of mountains dissected by narrow streams and covered by deciduous and conifer trees with abundant litter on the forest floor.

The topography and sampling locations are shown on Fig. 3. The maximum change in elevation of the sampling points is 135 m, and the largest basin area in the study site is 0.56 km^2. From late spring to autumn, the trees form a canopy over the hills, and the visibility of the sky from the ground is limited. On the south edge of the largest basin, the forest canopies are thin, and the nearby hills toward the southeast, in the direction of the FDNPP, are visible.

Some parts of the forests in the study site are not native. Thirty-one percent of Fukushima forests are planted (Fukushima Prefecture, 2010). Because no major forestry work had been conducted in the area after the accident, land use history was not considered in the analysis.

2.2. Soil Sample Collection

Soil samples were collected during the summer in 2016, 2017, and 2018. In 2016, samples were collected at locations 1 to 20, 44, and 45 (Fig. 3a) to cover accessible hillslope areas from the lowlands in a circular pattern. The 2017 sampling campaign sought to confirm anomalies observed in previous year and to check the Cs-137 concentration at the highest elevation by collecting samples at locations 11 to 14, 38, and 46. In 2018, the sampling activity focused on the southwest slope and the eastern side by collecting samples at 11 to 14, 21 to 37, 39 to 43, 45, and 46. Most sampling locations were on the southwest slope due to accessibility. In sum, there were 46 total sampling locations, multiple-year samples were collected at eight locations (averaged herein), and the total number of samples collected was 58. Coordinates were recorded at all sampling locations.

For sample collection, a sampler 5 cm in diameter and 30 cm long from Daiki Rika Kogyo Co., Ltd., Japan, was used. The circular tube was made of metal and contained a replaceable plastic liner. The sampler was tamped into the ground with a hammer. Once fully inserted, the sample was pulled out, and the plastic liner containing the soil was removed, sealed, and taken to the University of Tokyo.

2.3. Soil Property and Radioactivity Measurements

In the laboratory, each plastic tube was opened, photographed, divided into 2 cm-thick disks from the surface to a depth of 20 cm, and 2.5 cm thick disks from depths of 20–30 cm. All visible plant roots or rocks were removed. Each disk sample was placed on a plate, weighed, and dried in an oven for 24 hours at 105°C. The drying time was extended as necessary to achieve consistent dryness across the samples. The dried sample was reweighed, placed in a mortar, disaggregated, and particles larger than 2 mm were removed. Mass water content (%) and soil dry bulk density (g cm^{-3}) were calculated for each disk sample. Textural analysis (sand, silt, and clay) was performed on approximately one-half of all soil samples using the pipette method. The samples were selected so that various soil types, colors, locations, and elevations were represented. Organic matter in the soil samples was broken up by placing the sample into a beaker, adding hydrogen peroxide (H_2O_2), and placing the beaker into a 100 ºC water bath for 4–5 hours. The next day, sodium hexametaphosphate ($(NaPO_3)_6$) was added to the samples, which were shaken with a sonic homogenizer. As soon as the sample was placed onto the desk, suspended sediment was collected using a pipette at 20 s for sand (≥0.05 mm) and 4 hr for clay (≤0.002 mm) to determine the texture class of the sample. Each fraction was dried in the oven, weighed, and its fractional percentage determined. Silt fraction percentage was calculated from the results at 20 s and 4 hr. To verify the percentage of clay, selected samples were tested using SALD-7500nano (Nano Particle Size Analyzer, Shimadzu Corporation, Kyoto, Japan).

Processed samples were stored in polyethylene vials and sent to the Isotope Facility for Agricultural Education and Research, University of Tokyo, for analysis. Radioactivity levels were measured with a NaI(Tl) scintillation automatic gamma counter (2480 WIZARD2 gamma counter, PerkinElmer Inc., Waltham, MA, US), which was equipped with a well-type NaI(Tl) crystal 7.6 cm in diameter and 7.6 cm long, and covered with a 75 mm thick lead shield. Energy calibrations were performed using the 662 keV (kiloelectron volts) energy peak of gamma rays from Cs-137. For radiocesium, the detection limit was approximately 0.5 Bq. After each measurement, the radiation was separated into radiation emitted by Cs-137 and Cs-134 using the abundance ratio of Cs-137 to Cs-134 at the time of sampling. This ratio was obtained from the physical decay rates of the isotopes and the elapsed time from the accident to sampling, assuming that the ratio at the time of the FDNPP accident was 1:1 (Nobori, et al., 2013, Tanoi, et al., 2019). Although a gamma-ray spectrometer provides more precise Cs-137 measurement data, lower-resolution NaI with effective algorithms can be accurate, and it is preferred for its ruggedness, shorter time required for evaluation, and cost of operation (Burr and Hamada, 2009, Stinnett and Sullivan, 2013). The U.S. Environmental Protection Agency allows the NaI method for gamma-ray measurement (EPA, 2012).

In this study, Cs-137 values are reported in two units: Bq kg^{-1} or Cs-137 activity measurement per volume, and Bq m^{-2} or mass depth (Bq kg^{-1} × soil dry bulk density × sample thickness). Since soil bulk density varies across samples, mass depth indicates the functionality of soil bulk density as an explanatory variable, and it provides a means to compare concentration levels among samples with varied soil bulk densities (Kato, et al., 2012, Miyahara, 1991, Rosén, et al., 1999). Cs-137 values among samples were decay-normalized to 28 June 2016 (see Appendix 1), which enabled a comparison of measurements conducted on different dates, and the sum total of Cs-137 in the entire tube is called "core total."

Background Cs-137 contamination data before the FDNPP accident were unavailable for the study site. According to previous work, Cs-137 activities in Japanese soils varied from ≤15 to 100 Bq kg^{-1} before the accident (Table 3). Although the 100 Bq kg^{-1} measurement was an outlier, this value was used as the conservative background contamination level in the following analysis.

2.4. Digital Elevation Models (DEMs)

This study employed two DEMs. The 1-m resolution DEM was provided by the Forestry and Forest Products Research Institute, Japan. Its original datum was GCS JGD 2011 (Zone 9), and the data collection year was 2012. The 10-m resolution DEM was downloaded from the Geospatial Information Authority of Japan (https://www.gsi.go.jp/kiban/) website. Its file date was 1 October 2016, and the original datum was GCS JGD 2000. The coordinate projection of all GIS files, including DEMs, was set to UTM 54N (WGS 1984).

Analysis of geomorphic processes can be affected by spatial resolution (Claessens, et al., 2005, Martinez, et al., 2010, Miller, et al., 2015, Sørensen and Seibert, 2007). Using multiple DEMs enables researchers to identify resolution dependency of specific topographic features (Gallant and Wilson, 1996, Kim and Lee, 2004, Moore, et al., 1993).

The topographic parameters for analysis were selected based on the following assumptions.

1. **Elevation:** Soil particles with adsorbed Cs-137 move down a sloped surface, suggesting that Cs-137 concentration in surface soils would be higher at lower elevations (Martin, 2000, Roering, et al., 1999).
2. **Slope:** Slope influences the downward mass movement on a surface (Roering, et al., 1999).

3. **Upslope distance to the basin edge:** Assuming Cs-137 continuously moves down a sloped surface, the longer the upslope distance, the higher the Cs-137 concentrations (Komissarov and Ogura, 2017, Roering, et al., 2001, Roering, et al., 1999).
4. **Surface plan curvature and topographic wetness index (TWI):** Cs-137 moves into the subsurface by infiltration (Schimmack, et al., 1994, Schimmack, et al., 1989, Teramage, et al., 2014). Cs-137 concentrations would be higher where water ponds, and Cs-137 would migrate to a greater depth in the same temporal period, compared with other locations where water does not pond. Slope profile and surface plan curvature are influential factors in hydrology and soil transport on a sloped surface; hence, they would influence Cs-137 accumulation (Gessler, et al., 1995, Heimsath, et al., 1997, Momm, et al., 2012, Moore, et al., 1993, Tesfa, et al., 2009). The topographic wetness index (TWI) is frequently used in surface hydrology assessments (Hengl and Reuter, 2008). This index reflects water's tendency to accumulate at any point in a catchment (Quinn, et al., 1991), and it is calculated as the natural log of total upslope area divided by the tangent of hillslope gradient (Quinn, et al., 1991, Quinn, et al., 1995).

The elevation of sampling locations was extracted from the DEMs using the raster extract function in the R-package (R Core Team, 2015). SAGA GIS (Conrad et al., 2015) was used to compute slope and plan curvature because this function has multiple options for the curvature calculation setting. The method used for plan curvature calculation was the second-order polynomial based on the elevation values in nine surrounding cells (Zevenbergen and Thorne, 1987). The "D-Infinity Distance Up" tool of TauDEM was used to compute the upslope distance (Tarboton, 1997), which calculates the distance from each grid cell up to the ridge cells according to the reverse flow path directions. Here the "minimum" distance and "surface" (total surface flow path) distance calculation options were used. TauDEM also was used to calculate TWI values. All topographic calculations in SAGA and TauDEM were saved as .TIF files. The "raster::extract" function of the R-package was used to extract each topographic value for sampling locations.

2.5. Generalized Additive Models (GAM)

The sampling locations were influenced by terrain access, so they were not randomly selected or uniform, and the number of samples was small compared with the sampling area size. Thus, distance-based spatial analyses such as semivariograms would not be appropriate, and a regression approach was adopted.

Multiple regression methods (linear, polynomial, logarithm, and bi-splines) were run to check the relationships between Cs-137 measurements and the topographic parameters and the soil properties. The resulting regression plots showed fitting curves with multiple knots, and most of the topographic parameters had nonlinear, complex relationships with Cs-137 accumulation patterns. Thus, Generalized Additive Models (GAM) were employed. GAM replaces the linear predictor of a linear additive model with a sum of smooth functions of predictor variables (non-parametric) (Hastie and Tibshirani, 1990, Wood, 2017, Wood, et al., 2016). The smoothing parameter of GAM controls the trade-off between the smoothness of the fit and the closeness of the fit to the data (Wood, 2017; Eq. 1).

$$g(\mu_i) = A_i\theta + f_1(x_{1i}) + f_2(x_{2i}) + f_3(x_{3i}) + \cdots f_k(x_{ki}) \tag{1}$$

where $x_1, x_2, \dots, x_k$ are explanatory variables (predictors), $\mu_i \equiv \mathbb{E}(expected)(Y_i)$ and $Y_i \sim EF\left(\mu_i, \phi\right)$, Y_i are response variables, $EF\ (\mu_i, \phi)$ denotes an exponential family distribution with mean μ_i and a scale parameter ϕ, A_i is a row of the model matrix (parametric), and θ is a corresponding parameter vector. Finally, f_j are smooth functions (non-parametric) of the covariates, x_k. In GAM algorithms, models are estimated by minimizing squared errors with an increasing penalty as the curves become less smooth.

GAMs allow flexible specification of the response variable dependence on predictors according to the smooth function rather than parametric relationships (Wood, 2017). Because a smooth function is estimated for each covariate, when multiple predictors are included in a model, it is a sum of these functions and a constant.

GAM users can examine the significance and the model fit of each predictor and the overall model performance with multiple indicators (model knots, effective degree of freedom, F-statistic, p-value, R^2, and deviance explained percentage). Deviance explained percentage is the proportion of the total deviance explained by the model. This serves as a generalization of R^2 in GAM. While overfitting can be a potential problem of GAM (Friedman and Stuetzle, 1981), GAMs work well when users aim to detect the significance of predictors, and the baseline relationship between the predictors and the response variable in a complex model environment (Hastie and Tibshirani, 1990, Linnik, et al., 2020, Tesfa, et al., 2009).

3. Results

All primary data collected in the field campaign, processed in the laboratory, and derived from the DEMs are summarized in Appendix 2.

3.1. Cs-137 Concentration Distributions Among Core Samples

Fig. 4a shows the binned distributions of core total Cs-137 values in kBq kg^{-1} (red) and kBq m^{-2} (grey), as well as their means (Fig. 4b in a log scale). When measured in kBq kg^{-1}, the Cs-137 values clustered in six bins, and 41% of the core samples were in the 100–300 kBq kg^{-1} interval (Fig. 4a: red). When measured in kBq m^{-2}, Cs-137 values spread across 13 bins (Fig. 4a: grey). The average total core Cs-137 values among these samples were 267 kBq kg^{-1} and 1,075 kBq m^{-2}.

Cs-137 activities exponentially decreased with depth in both kBq kg^{-1} and kBq m^{-2} (Fig. 5a). These vertical profiles are similar to the results reported in previous studies (Fujii, et al., 2014, Koarashi, et al., 2012, Matsunaga, et al., 2013, Takahashi, et al., 2015, Tanaka, et al., 2012, Teramage, et al., 2014). The current samples were collected five to seven years after the FDNPP accident, and the soils still held the largest amount of Cs-137 in the uppermost layer. The average depth of 90% concentration (90% of the entire Cs-137 in a core sample) was 6.1 cm in kBq kg^{-1} and 6.9 cm in kBq m^{-2}. Standard deviations of Cs-137 activities were up to 115 kBq kg^{-1} and 335 kBq m^{-2} in the upper 2 cm depth (black dots in Fig. 5b and Fig. 5c). The relative variability among samples (COVs: coefficient of variations) was below 100% in the top layer, and COVs increased toward the 14–16 cm depths and decreased again for both units (grey dots in Fig. 5b and Fig. 5c).

3.2. Soil Properties

Fig. 6 displays the averages of mass water content (%) and soil dry bulk density (g cm^{-3}) for each depth layer. Gravel (below the mid-depth from two disks) and visible roots (at the ground surface from several samples) were removed, which decreased the dry bulk densities of select samples.

Soil texture affects the amount of adsorbed Cs-137 per unit mass of soil particles and accumulation patterns of Cs-137 in soils (Bennett et al., 2005; Giannakopoulou et al., 2007; Korobova et al., 1998; Walling and Quine, 1992). On average, the tested soils contained >50% sand, and most of the samples were in the categories of sand, loamy sand, sandy loam, and loam (Appendix 2).

The average mass water content percentage at the ground surface was above 100% (Fig. 6a). The standard deviations of water content in the uppermost soil layers were >50% and the deviation percentages decreased with depth. Some samples collected near the surface exceeded field capacity, likely due to poor drainage, soil texture, and/or high organic content.

Soil dry bulk density and its standard deviation increased with depth (Fig. 6b). The average dry bulk density of all disk samples was 0.45 g cm^{-3}, and the densities ranged from 0.06 g cm^{-3} to 1.43 g cm^{-3}. The Japanese agricultural soil profile physical properties database, Solphy-J, compiled data for 1800 categories of Japanese soils (Eguchi, et al., 2011). This database shows that the soil dry bulk densities of Japanese orchard soils range from 0.80–1.44 g cm^{-3}. Fujii, et al., (2014) collected soil samples to 20 cm depth at five locations in Fukushima forests, and these soil dry bulk densities ranged from 0.3–0.7 g cm^{-3}. The relatively low bulk density in this study agrees well with previous work.

3.3. Cs-137 Concentration Distribution on Representative Slope

Figs. 7 and 8 organize the core total Cs-137 concentration of all samples by elevation and slope. Migration head depths have been added to Fig. 7, defined as the depth at which Cs-137 activity (Bq kg^{-1}) decreased to the conservative background activity level (i.e., 100 Bq kg^{-1}). This study considers the head depth as the deepest subsurface migration point of the FDNPP-derived Cs-137. These figures provide an overview of Cs-137 distribution patterns on the hillslopes. Numbers 1–4 are added to the graphs to indicate the highest concentration samples in Bq m^{-2}. The elevation data were extracted from the 10 m resolution DEM.

Cs-137 activities in kBq m^{-2} unit increase with elevation (p-value is 0.03), but this trend was not observed for Cs-137 concentrations in kBq kg^{-1} (Fig. 7). The migration head depths of three of the samples with the highest Cs-137 concentrations had reached the end of the sampler (30 cm), and the average migration depth among all samples was 21.7 cm. Two of the four highest Cs-137 concentrations were at the highest elevation and near the bottom of a hill (Fig. 7), and they were locations with relatively low slopes (Fig. 8). The remaining two samples with the highest Cs-137 concentrations were at 24–26° slopes, which are two of the steepest sampling locations. Elevation and slope do not appear to explain the distribution of Cs-137 concentration, suggesting that additional topographic parameters may be required.

3.4. GAM Assessment

Model assessment will focus on eight parameters: Cs-137, five topographic parameters, and two soil properties. This study used mgcv in the R-package (Wood, et al., 2016) for GAM calculations. The model setting was consistent for all model runs, except rotating predictors (see Appendix 1).

First, GAMs were run with a single topographic parameter or one of the soil properties. Then models with parameter combinations were run to assess the interactions among the parameters. Combinations with more than three parameters were not tested to avoid overfitting and to identify parameters with distinct influences on Cs-137 concentrations. The total number of possible combinations was 63—combinations of seven parameters, including five topographic parameters (elevation, slope, upslope distance, plan curvature, and TWI), and two soil properties (water content and soil dry bulk density), not considering the parameter orders (Fig. 9). Among the 63 combinations, three were only soil properties (combinations of two properties), 25 were only topographic parameter(s) (combinations of five predictors), and the remaining 35 were mixed soil properties and topographic parameters. Then, the same GAM with topographic parameter(s) was executed four times against Cs-137: topographic parameters extracted from the (1) 1 m and (2) 10 m DEMs, and with units of (3) Bq kg^{-1} and (4) Bq m^{-2}. Soil parameters are not affected by DEM resolutions (Fig. 9).

GAMs were executed against each depth layer to check model performance as affected by changes by depth. Topographic parameters have one distinct value for an entire core sample, such as elevation and slope. Thus, when a model included a topographic parameter, the model check was a "one-to-many" relationship (topographic parameters to Cs-137 in multiple depth layers). Soil properties had a measurement for each depth layer. Thus, when a model included a soil property, the prediction was a "one-to-one" relationship (soil property in a depth layer to Cs-137 in the depth layer).

GAM accuracies were evaluated by three indicators: Akaike Information Criteria (AIC), Generalized Cross Validation (GCV), and R^2 (see Appendix 1). These model parameters were extracted from mgcv outputs in the R-package. The AIC is a weighted sum of the log-likelihood of the model and the number of fitted coefficients. The lower the AIC indicates a better model fit (Bivand, et al., 2008). GCV is a simplified version of cross validation that checks model fit by removing one data point at a time. GCV can be used in a similar way as AIC to measure the relative performance of multiple models.

Identifying outliers is vital for understanding model errors and capturing influential factors not included in the model. Cook's distance method was used for outlier identification (Cook, 1977; see Appendix 1). Cook's distance identifies influential data points by checking how the fitted model parameters change when an outlier data point is removed. Cook's outliers were extracted from linear regression summary plots using the R-package (Stevens, 1984).

There was no reference data from other sites to validate the model prediction accuracy. Therefore, Cs-137 concentrations were reverse-predicted by applying the two best-performing prediction models to the original data. Here, mgcv's "predict.gam()" in the R-package was used to generate the predictions.

3.4. GAM Performance

In Tables 4 and 5, the percentage of deviance explained shows the average values for the 30 cm depth for single-parameter model results. The p-value columns show the number of depth layers in which the average p-values were equal to or less than the significance threshold ($p \leq 0.05$; e.g., "4/14" means that four depth layers had $p \leq 0.05$.). Table 4 includes the model results with each topographic parameter that varied with DEM resolution. Table 5 displays the model results with each soil property parameter, whose values were unaffected by the DEM resolution. None of the single parameter models returned average deviance explained percentages greater than 36%, which was the model with water content. The lowest average p-value was 0.05, which was also the model with water content. Among topographic parameters, TWI was the most effective predictor with the 1 m DEM (27%), and slope was the most effective predictor with the 10 m DEM (28%). Elevation and slope explained Cs-137 deviance better with 10 m DEM than with 1 m DEM. Topographic parameters explained Cs-137 deviance at higher percentages in Bq kg^{-1} units than in Bq m^{-2} units, except plan curvature. Soil properties explained Cs-137 deviance at higher percentages than did the topographic parameters. Like the topographic parameters, the soil properties model explained Cs-137 deviance at higher percentages in Bq kg^{-1} units than in Bq m^{-2} units.

Figs. 10 and 11 display the deviance explanation percentages of GAMs with combinations of parameters, where the red and gray dots represent the deviance explanation percentages of Cs-137 in Bq kg^{-1} and Bq m^{-2} units, respectively. The average correlation index between the average deviation explanation percentages and p-values throughout the depth was −0.64. That is, higher explanation percentages returned lower p-values.

The combination parameter models explained Cs-137 deviance in Bq kg^{-1} (red dots) at higher explanation percentages on average than deviance in Bq m^{-2} (grey dots) for both DEMs, and all six figures showed similar vertical S-curves (Figs. 10 and 11). The deviance explained percentages of some models were over 75% for the top layer; the percentages explained decreased with depth, then increased again toward the 12-14 cm depth. These S-shaped curves resemble the vertical profiles of the COVs of Cs-137 measurements (Figs. 5b and 5c), and the curves were observable for models with only soil properties and only topographic parameters.

The most effective parameter combinations for explaining Cs-137 deviance are summarized in Table 6. The rows are separated into the model combinations with a mix of soil and topographic parameters, and the model combinations with only the topographic parameters. The most effective combinations for predicting Cs-137 deviance were "water content + bulk density + elevation" for models with both 1 m (53.56%) and 10 m (54.03%) DEMs. The most effective topographic parameter combinations were "slope + plan curvature + TWI" when using the 1 m DEM (40.62%) and "elevation + slope + upslope distance" when using the 10 m DEM (46.70%). The combination models returned higher explanation percentages using the 10 m DEM and Cs-137 in Bq kg^{-1} units.

Two models with the highest explanation percentages in Table 6 are identified as Model A and Model B. These will be used for reverse prediction accuracy checks.

The two models in Table 6 that had the best performance were applied to the original data to reverse-predict Cs-137 concentrations with the 10 m DEM, and model accuracies were checked. Regression analyses between the actual and predicted Cs-137 values returned R^2=0.54 for Model A with soil properties and elevation (Fig. 12a). Model B with only the topographic parameters returned lower R^2=0.25 (Fig. 12b), overestimating two data points at 400–1000 Bq kg^{-1}. With increased depth, model fit (AIC and GCV) continues to improve while the Cs-137 standard deviations decrease (Figs. 12c and 12d). The explanation power of the model (deviance explained and R^2) was the highest at the mid-depth region, where the relative variance of Cs-137 was the largest (Figs. 5b and 5c).

Four outliers were identified on the basis of Cook's criterion. Two of the outliers (samples 37 and 38 on Fig. 3) were at the highest elevation on the basin ridges with a flat surface. The third outlier (sample 23 on Fig. 3) was at a location with a lower TWI (in the first quantile) and a 26° slope. This sample did not show extreme values in Cs-137, water content, or soil dry bulk density, but the migration head depth of the sample was one of the deepest at 16 cm. The fourth outlier (sample 32 on Fig. 3) was near the basin edge and at a location with a 15° slope, and concave curvature. This sample had the highest water content in the uppermost layer (0–2 cm). Outlier samples 23 and 37 on Fig. 3 had the highest Cs-137 concentrations in Bq kg^{-1}.

4 Discussion

4.1. Explanatory Power of GAM

The GAM results demonstrated about 50% of Cs-137 deviance was explained by three parameters (Table 6). Model performance might be improved by including factors such as surface vegetation and subsurface organic matter (Claverie, et al., 2019, Doerr and Münnich, 1989, Dumat, et al., 1997, Dumat, et al., 2000, Fan, et al., 2014, Korobova, et al., 2016, Mabit, et al., 2008, Staunton, et al., 2002, Takenaka, et al., 1998, Tatsuno, et al., 2020). Topography itself did not explain the entire Cs-137 concentration patterns in the forest; however, the influence of topography on Cs-137 concentration patterns was measurable.

Elevation and slope are commonly used in geomorphic assessments of Cs-137 contamination (see references above). GAMs with only elevation or slope explained Cs-137 concentrations at less than 28.31% in either unit (Bq kg^{-1} or Bq m^{-2}). Despite its less significance for explaining Cs-137 deviance as a single parameter, elevation appeared seven times in the eight best-performing models (Table 6). The best models in all four categories (two by Cs-137 units; two by DEM resolutions) in Table 6 consisted of water content, soil dry bulk density, and elevation. The topographic parameters in the remaining four best-performing models varied. Elevation did explain Cs-137 deviance; however, its effects did not materialize by itself in the model result and needed to be combined with other supporting topographic features or soil properties. This indirect effect on Cs-137 deviance is true for other topographic parameters because the combination models returned higher explanation percentages for any single parameter model. These results show that when the models account for both the characteristics of soils, as the Cs-137 retention medium, and topography, as the Cs-137 translocation driver, their prediction power increases.

At depths of 12-18 cm, the explanation percentages for the GAMs were above 75% (Figs. 10 and 11), and Cs-137 displayed the largest COVs around the same depths (Figs. 5b and 5c). Because those depths were just above the average migration head depth, 21.7 cm, it is hypothesized that the downward movement of Cs-137 was affected by topography, and that these effects are retained as particles with adsorbed Cs-137 continued their interstitial movement downward.

The vertical profiles of the GAM explanation percentages were similar for soil properties and topographic parameters throughout the depth (Figs. 10 and 11). Pearson's Correlation Indices were calculated between the soil properties and topographic parameters. The only pairs that showed a correlation greater than 0.5 were water content at 12-16 cm depth vs. TWI, and soil dry bulk density at 2-4 cm vs. upslope distance. The explanation percentages by soil properties and topographic parameters were the result of a nonlinear functional relationship between them.

The migration head depths in Fig. 7 did not show a distinct trend with elevation; however, the migration head depths for eight samples had already reached 30 cm deep. Table 7 compares the depths at which 90% of the total Cs-137 concentration in soil samples was measured (not migration head depths) for the CNPP accident (Ivanov, et al., 1997) and those reported here. The present results show that Cs-137 concentrations had migrated deeper into the subsurface than in the region affected by the CNPP accident.

4.2. Model Fit Analysis

The two GAMs with the best overall performance, Model A with soil properties and elevation and Model B with only topographic parameters in Table 6, were explored to assess their predictive ability. While each GAM was run against all 14 depth layers, only the outputs for five depth layers are discussed here. These are 0-2 cm, 4-6 cm, and 8-10 cm to display model fits in the soils close to the surface where Cs-137 was concentrated, 14-16 cm to display the model fits in the mid-depth, and 20-22.5 cm to display the model fits at the average migration head depth. Fig. 13 lists the fitted smoothing parameters of the model predictors for these two models.

For each plot in Fig. 13, the x-axis is the model predictor and its value range, and the y-axis is the smoothing parameter. The numbers on the y-axis indicate the partial residuals from the fit. Thus, the y-axis demonstrates an increase or decrease of the response values against its predicted mean. The grey area represents the 95% confidence interval range, and the vertical red dashed line indicates the predictor value at which the smoothing parameter is zero–mean.

The fitted curves for Model A (fitted smooth) show that water content and elevation were positively related to Cs-137 (Figs. 13a and 13c). Soil dry bulk density was negatively related to Cs-137 (Fig. 13b). Cs-137 increases as water content increases, although the increasing pattern is not linear in two depth intervals (Fig. 13a). The Cs-137 increases above the mean at around the water content 50–120%. The samples in this study contained soils with mass water content above 100%, and those soils had elevated Cs-137, when they were dried. Cs-137 decreased below the mean at a soil dry bulk density around 0.2-0.55 g cm^{-3} (Fig. 13b). GAMs returned higher explanation percentages when run against Cs-137 in Bq kg^{-1} unit than in Bq m^{-2} (Tables 4 to 6). These results indicated that soil dry bulk density, included in mass depth (Bq m^{-2}) calculation, was not a significant factor in explaining Cs-137 concentrations. The model-fitted curves in Fig. 13b show the negative linear relationships between soil dry bulk density and Cs-137 predictions. Since soil dry bulk density increases with depth, Cs-137 is concentrated in low density soils close to the surface. In this study site, soil dry bulk density had an influence on Cs-137 concentrations, which appeared when density was combined with other model parameters. Cs-137 and elevation showed positive linear correlations or U-shape fitted curves depending on the depth (Fig. 13c). The bottom of the U-shape was around the elevation of 610 m. One sample collected at the elevation of 613 m contained the highest core average soil dry bulk density, which also had the lowest core total Cs-137 concentration and the highest dry bulk density in the top 0-2 cm layer.

The fitted curves for Model B show that elevation was positively related to Cs-137 (Fig. 13d), and slope was negatively related to Cs-137 except in the 0–2 cm depth (Fig. 13e). Elevation was a common predictor in both models (Figs. 13c and 13d). The elevation's fitted curves in the two models showed that the same predictor's fitted smooths could vary depending on its relation to other predictors in the model. Slope showed a fitted curve near the surface (0–2 cm depth) with an increasing trend, but an opposite trend from other layers below (Fig. 13e). Three samples with the highest Cs-137 concentrations in the 0–2 cm depth were found at slopes steeper than 15 degrees. These samples pushed the trend upwards toward a steeper slope in the 0–2 cm depth range. Slope presented the fitted curves with multiple knots between 5–25 degrees in the 14–16 cm depth. Yet, the fitted smooths did not move away from the mean, indicating that slope in this range contributed little to Cs-137 concentration. Upslope distance contributed to a Cs-137 increase toward the shortest upslope distance (at the ridge area) and the longest upslope distance (hill bottom area; Fig. 13f). The sample with the highest core total Cs-137 concentration was about 10 m below the ridge edge. Higher Cs-137 concentrations at the ridge area is counter-intuitive because Cs-137 was expected to move downslope with surface soil creep or runoff. The Cs-137 concentrations in five samples collected at the shortest upslope distances did not show any apparent relationships with water content, soil dry bulk density, or other topographic features.

On the basis of the model fits, predictions for the Cs-137 concentrations in this study site are as follows.

1. Cs-137 concentrations generally increase with elevation, but the increase is not linear (Fig. 7, Fig. 13c).
2. Higher Cs-137 concentrations can be found at the highest elevation near the ridge or hill bottom (Figs. 13c and 13f).
3. Higher Cs-137 concentrations will be observed at the locations with lower slopes, which could include flat areas at the ridge and near the hill bottom (Fig. 13e).
4. Soils with higher water content might contain higher Cs-137 concentrations once dried (Fig. 13a)
5. Higher Cs-137 concentrations can be found in lower soil dry bulk density close to the surface. Exceptions can be found at locations where water does not pond, even though soil dry bulk density is higher (Figs. 13b and 13c).

4.3. The Effect of DEM Resolution

The ratios between topographic parameter values extracted from the two DEMs are shown in Table 8. The last column of Table 8 indicates the DEM resolution where each topographic parameter appeared in the best performing GAM models (Table 6). The elevation and slope values were consistent between the 1 m and 10 m DEM, indicating that elevation did not change drastically over distances less than 10 m. Upslope distance had the largest difference between the DEMs. Plan curvature and TWI, which influence surface water ponding, appeared in the best performing models with the 1 m DEM. Upslope distance performed better with the 10 m DEM, but the average upslope distance was four times greater with the 10 m DEM.

4.4. Study Contribution

This study employed empirical approaches to derive predictive relationships among Cs-137 and soil property data and local topography. The statistical results show the power of detecting co-functionalities of topographic predictors on Cs-137 accumulations on the ground surface and with depth, which could enhance the understanding of the geomorphic mechanisms governing Cs-137 accumulations in a forested area. While model prediction errors might depend heavily on factors not included in this study, the current approach proposes a methodology to partition observed Cs-137 concentrations into explainable and un-explainable portions. The methodology and results presented here could contribute to ongoing research on understanding the distribution of radioactive contamination in complex terrains.

4.4. Study Limitations

In this study, the Cs-137 measurement began in 2016, and the physical translocation of Cs-137 prior to 2016 was not considered as no soil monitoring was conducted. The only data available were the initial Cs-137 deposition estimates from the Japanese government and the U.S. Department of Defense (MEXT, 2011), which was 1000–3000 kBq m^{-2} as of July 2011. The Cs-137 values are decay-normalized and do not consider the physical movement of Cs-137 over the three-year sampling period. While the effects of precipitation magnitude and frequency cannot be ignored, all soil sampling campaigns were conducted at approximately the same time of year (i.e., after the rainy season). All sampling campaigns avoided intense precipitation immediately prior to sample collections.

5. Conclusions

Following an earthquake near the northeast coast of Honshu, Japan, and a subsequent tsunami, the FDNPP suffered a catastrophic failure and a radioactive plume, including Cs-137, was released into the atmosphere. While much previous research focused on documenting Cs-137 concentrations in nearby environments, there has been no systematic and quantitative study that examined the effect of topographic indices and soil properties on the concentration and distribution of Cs-137 from this accident. To address this issue, 58 soil core samples were collected over a three-year period from the ground surface to depths of 30 cm in Iitate Village, a forested region located 35 km northwest of the FDNPP. The Cs-137 concentrations for these samples were assessed along with various topographic indices derived from digital elevation models and soil properties. Generalized Additive Models (GAM) were then employed to quantitatively determine the singular and collective impact of topography, soil properties, and digital elevation model resolution on predicting the concentration of Cs-137 within this landscape. The primary conclusions of the study are as follows.

1. In general, Cs-137 activities were highest near the ground surface and decreased exponentially with depth. The average depth of 90% concentration was 6.1 cm in kBq kg^{-1} and 6.9 cm in kBq m^{-2}, and the average migration depth for all samples was 21.7 cm.
2. Higher concentrations of Cs-137 occurred at the highest elevations or near the bottom of hills.

3. Elevation, slope, upslope distance, plan curvature, and TWI were derived for each sample location using 1 m and 10 m DEMs. Resolution of the DEM produced marked differences in the upslope distance, plan curvature, and TWI indices determination, which then affected the Cs-137 predictions.
4. Using two units for Cs-137 concentration, five topographic indices, and two soil properties, 63 GAMs were evaluated using one- to three-parameter combinations and two DEMs with different resolutions, which were assessed using several criteria. For the single parameter models, none returned average deviance explained percentages greater than 36%. In contrast, the most effective model combinations for predicting Cs-137 deviance were "water content + bulk density + elevation" for the 1m (53.56%) and 10 m (54.03%) DEMs, given the empirical data reported herein. The most effective topographic parameter combinations were "slope + plan curvature + TWI" when using the 1 m DEM (40.62%) and "elevation + slope + upslope distance" when using the 10 m DEM (46.70%). Concentrations of Cs-137 within this landscape were reverse-predicted using the best two GAMs (Model A: "water content + bulk density + elevation" and Model B: "elevation + slope + upslope distance"). For the data reported herein, Model A outperformed Model B.

While this study focused on a small forested region affected by the FDNPP accident, the results clearly show that Cs-137 concentrations in soils are strongly affected by landscape topography. This topographic effect should be given careful consideration in the use of anthropogenic radionuclides as environmental tracers and in the assessment of current and future environmental risks due to nuclear power plant accidents.

Author contributions

Yasumiishi, M. conceived and designed the project; Yasumiishi, M. and Nishimura, T. conducted field data collections and laboratory analysis; Yasumiishi, M. conducted data analysis and graphing; Nishimura, T., Aldstadt, J., and Bennett, SJ. provided critical feedback on data analysis; Yasumiishi, M. drafted the manuscript; Bittner, T. advised on data concepts. All authors provided critical feedback to finalize the manuscript.

Competing interests

The authors declare that they have no conflict of interest.

Acknowledgments

This study was supported by the following awards: The NSF East Asia and Pacific Summer Institutes (EAPSI) 2016 program [award number: 1614049], the NSF Doctoral Dissertation Research Improvement Award - Geography and Spatial Sciences Program (DDRI-GSS) [award number: 81809], and the College of Arts and Sciences Dissertation Fellowship of the University at Buffalo. Field sampling, soil sample lab tests, and radioactivity measurements were accomplished with the support of the Laboratory of Soil Physics and Soil Hydrology, Graduate School of Agricultural and Life Sciences, the University of Tokyo, Japan. Forestry and Forest Products Research Institute, Japan provided the 1-m resolution DEM. Mr. Kinichi Okubo, a farmer in Iitate Village, kindly provided his land for this research.

Appendix 1 Equations

R-Package mgcv GAM Model Settings

Model ← gam(Cs-137 ~ s(x_1) + s(x_2) + s(x_3), data=data, method="REML", bs="cr", family=Gamma(link=log)) where 's' is a smooth function of covariates of the predictor, 'method' specifies a fitting method, and 'bs" specifies basis function ("cr", cubic splines, in this model). 'family' specifies a response variable distribution type. 'link' solves the problem of using linear models with non-normal data by linking the estimated fitted values to the linear predictor (Clark, 2013). This study used 'Gamma(link=log)'to address complex, non-linear interactions among predictors.

Cs-137 Decay Equations

The Cs-137 decay constant is calculated as follows (Eq. A1):

$$\lambda = \frac{\ln 2}{T\frac{1}{2}} \qquad \text{(A1)},$$

where λ is the decay constant and $T_{1/2}$ is the half-life. The half-life of Cs-137 is 30.17 years; thus, λ = 0.023 year^{-1}. The radioactive decay formula is as follows (Eq. A2):

$$N_0 = \frac{Nt}{e-\lambda t} \qquad \text{(A2)},$$

where N_0 is the original Cs-137 value, Nt is the Cs-137 value after time t, and λ is the decay constant (IAEA-TECDOC, 2003).

Akaike Information Criterion (AIC)

$$AIC = -2l(\hat{\theta}) + 2p \text{ (Wood, 2017)} \qquad \text{(A3)},$$

where $l(\hat{\theta})$ is log-likelihood and p is the number of identifiable model parameters (usually, the dimension of θ).

Generalized Cross Validation (GCV)

$$V_g = \frac{n\sum_{i=1}^{n}(y_i - \hat{f}_i)^2}{[\mathrm{n}-\mathrm{tr(A)}]^2} \text{ (Hastie, et al., 2009, Wood, 2017)} \qquad \text{(A4)},$$

where V_g is the generalized cross-validation score, y_i is the excluded data, $\hat{f}$ is the estimate from fitting to all the data, and $\mathrm{tr(A)}$ is the mean of the model matrix A_{ii}. The matrix measures the degree that the ith datum influences the overall model fit.

Cook's Outliers

$$D_i = \frac{\left(\hat{\beta}_{(-i)} - \hat{\beta}\right)' \mathrm{X'X} \left(\hat{\beta}_{(-i)} - \hat{\beta}\right)}{(p+1)\hat{\sigma}^2} \quad i = 1, 2, \dots n \text{ (Cook, 1977, Stevens, 1984)} \qquad \text{(A5)},$$

where $\hat{\beta}$ is the vetor of estimated regression coefficients with the i th data point deleted, p is the number of predictors, $\hat{\sigma}^2$ is the residual variance of the full dataset.

Appendix 2 Summary of all primary data collected.

Summary of topographic indices for all core sample locations (58 core samples, 46 locations)

Core	Elevation (m)		Slope (degrees)		Upslope Distance		Plan Curvature		TWI	
	1 m DEM	10 m DEM	1 m DEM	10 m DEM	1 m DEM	10 m DEM	1 m DEM	10 m DEM	1 m DEM	10 m DEM
1	549	557	26.4	18.7	43.5	42.0	-0.01	0.00	2.42	4.99
2	546	553	8.9	20.6	52.3	42.0	-0.83	0.00	3.65	4.99
3*	546	553	8.9	20.6	52.3	42.0	-0.83	0.00	3.65	4.99
4	543	543	22.2	9.7	10.4	77.5	-0.02	-0.11	2.02	9.60
5	545	544	20.9	16.4	5.4	67.4	-0.07	0.00	2.64	4.79
6	539	540	11.1	6.0	14.0	99.0	0.38	0.00	2.99	8.83
7	547	547	10.8	11.1	14.4	156.7	-0.19	0.00	2.98	8.12
8	545	540	26.4	7.4	37.5	56.3	-0.01	0.01	1.92	6.85
9	537	539	6.8	3.5	1.0	101.0	-0.27	0.02	-0.06	6.59
10	539	541	4.5	10.0	1.0	85.8	0.28	0.01	1.52	5.81
11	540	545	15.1	5.1	8.3	67.7	0.01	0.00	3.00	5.52
12	544	546	22.0	9.4	12.5	48.2	0.05	0.02	1.10	5.17
13	543	548	13.3	5.1	19.5	70.4	-0.26	-0.04	0.85	7.72
14	540	546	13.2	6.7	18.8	79.6	-0.09	0.00	3.14	5.61
15	552	553	7.6	10.9	4.1	63.2	-0.13	-0.02	2.74	6.35
16	553	555	12.8	12.1	5.6	58.5	-0.76	0.00	1.18	5.66
17	557	558	13.3	11.3	4.1	63.4	-0.13	-0.02	1.88	6.15
18	558	558	8.8	15.4	49.6	63.4	0.00	-0.02	2.80	6.15
19	562	564	7.6	14.2	70.6	136.7	0.00	-0.02	2.59	5.35
20	562	561	11.8	10.6	3.5	69.3	-0.04	-0.13	1.36	10.67
21	560	563	11.8	16.9	14.3	58.8	0.00	-0.02	1.24	5.72
22	566	570	15.8	13.4	59.8	105.6	-0.13	0.01	1.00	5.12
23	581	584	15.9	25.8	33.9	274.2	0.19	0.01	1.57	4.57
24	581	579	20.0	17.3	14.0	126.1	0.09	-0.02	1.87	5.70
25	590	595	21.4	27.8	31.6	247.6	0.24	0.00	0.53	4.08
26	590	595	11.2	18.0	5.7	102.3	0.02	0.01	1.74	4.72
27	614	618	13.4	12.2	129.2	137.4	0.13	0.02	0.22	5.78
28	605	609	13.3	19.0	21.0	168.9	0.32	-0.01	0.10	6.44
29	612	613	16.8	16.7	65.8	153.4	-0.02	-0.03	0.88	8.18
30	626	627	21.8	18.0	88.3	137.1	-0.06	0.02	0.88	4.37
31	617	616	26.4	23.2	11.8	156.8	-0.03	0.01	1.08	4.57
32	632	634	22.5	15.2	65.1	93.9	0.03	-0.03	1.27	7.18
33	642	642	18.3	16.3	61.0	81.0	0.16	-0.04	0.44	6.83
34	649	650	21.7	19.9	4.1	72.5	-0.01	-0.01	1.69	6.03
35	666	669	21.4	26.7	47.7	45.1	-0.10	-0.04	0.80	5.39

36	662	663	26.6	24.5	10.4	62.5	0.03	0.03	-0.14	4.34
37	673	673	8.1	9.8	7.4	10.8	-0.06	-0.02	3.21	4.39
38	676	673	8.9	3.1	6.8	0.0	0.06	0.15	3.73	4.64
39	552	558	31.3	24.1	23.1	21.7	0.06	0.00	0.24	3.85
40	555	563	35.1	12.9	23.1	21.7	-0.09	0.00	1.17	3.92
41	557	558	34.1	23.8	15.1	21.7	-0.11	0.00	1.18	3.92
42	564	561	26.9	12.2	4.9	10.7	-0.02	0.01	1.32	4.39
43	563	562	18.1	12.4	3.5	0.0	-0.07	0.15	2.51	4.20
44	554	553	21.9	23.2	34.3	37.5	0.00	0.03	2.26	3.50
45	551	544	26.7	23.4	27.2	60.7	0.04	0.01	1.91	4.52
46	537	540	6.9	1.5	58.6	108.9	0.01	-0.01	3.62	11.95

Summary of data collected for all core sample locations. Units include Cs-137: Bq kg^{-1}, Dry Bulk Density: g cm^{-3}, Mass Water Content: %, Sand, Silt, and Clay content: %. Among 58 core samples, multi-year samples were decay normalized and averaged.

Core	Parameters	Depth Increment (cm)													
		0-2	2-4	4-6	6-8	8-10	10-12	12-14	14-16	16-18	18-20	20-22.5	22.5-25	25-27.5	27.5-30
1	Cs-137	178093	23459	7406	3155	2025	1159	1155	668	273	83	93	39	32	29
	Bulk Density	0.19	0.16	0.30	0.24	0.46	0.31	0.48	0.75	0.43	0.51	0.68	0.62	0.51	0.82
	Water Content	21.81	27.41	31.70	33.75	33.53	30.55	26.22	25.70	24.67	23.80	20.99	16.57	17.70	17.03
2	Cs-137	216579	142177	36546	12138	5428	2126	1211	643	274	88	45	186		
	Bulk Density	0.17	0.15	0.15	0.15	0.28	0.48	0.31	0.35	0.28	0.22	0.28	0.16		
	Water Content	20.27	35.78	39.93	36.70	39.84	40.29	40.69	46.13	46.45	47.93	45.64	45.42		
3	Cs-137	18852	8612	9292	1190	5280	3410	821	365	299	*	259			
	Bulk Density	0.29	0.24	0.19	0.33	0.32	0.36	0.24	0.30	0.34	*	0.24			
	Water Content	32.58	40.38	57.63	75.81	44.92	46.31	48.64	49.36	48.87	*	79.51			
4	Cs-137	135696	41670	1171	114	139	79	55	108	75	21	19	32	18	7
	Bulk Density	0.38	0.62	0.72	0.91	0.66	0.72	0.81	0.70	0.79	0.84	0.81	0.98	0.97	0.87
	Water Content	51.94	41.88	36.37	34.24	35.73	35.09	34.92	35.73	34.85	30.90	31.40	31.81	32.23	31.27
5	Cs-137	95741	7751	2748	2550	1432	447	259	212	204	160	307	67	20	21
	Bulk Density	0.27	0.29	0.30	0.37	0.54	0.50	0.47	0.25	0.42	0.36	0.36	0.51	0.42	0.49
	Water Content	47.51	40.74	40.29	40.31	32.86	34.80	43.83	49.22	47.95	48.12	42.28	45.02	40.27	35.44
6	Cs-137	84442	8070	3850	1710	447	352	199	92	59	47	37	29	24	79
	Bulk Density	0.31	0.39	0.36	0.44	0.69	0.44	0.50	0.82	0.59	0.48	0.82	0.67	0.92	0.81
	Water Content	59.30	56.10	53.01	44.65	44.85	41.70	40.04	38.90	38.71	38.87	36.67	37.58	33.94	34.09
7	Cs-137	78211	30932	9971	2045	2225	511	209	116	124	46	30	17	13	14
	Bulk Density	0.23	0.23	0.28	0.38	0.29	0.53	0.49	0.52	0.74	0.67	0.81	0.86	0.66	1
	Water Content	171.93	156.49	99.71	75.77	79.94	81.53	64.43	42.91	41.14	32.73	30.26	30.19	27.88	21.61
8	Cs-137	413156	104035	57107	31112	14496	7292	1444	779	588	1099	808	628	387	201
	Bulk Density	0.06	0.06	0.07	0.14	0.21	0.24	0.30	0.31	0.30	0.38	0.40	0.37	0.26	0.46
	Water Content	207.62	205.80	162.36	86.03	43.55	40.56	42.13	40.94	36.91	34.28	35.26	37.51	37.89	36.09
9	Cs-137	200855	22354	4027	2430	1350	587	288	163	84	80	92	57	115	75
	Bulk Density	0.11	0.18	0.22	0.31	0.24	0.31	0.26	0.47	0.46	0.30	**	**	**	**

	Water Content	114.88	95.46	87.89	90.11	86.05	82.57	74.20	75.10	71.79	80.13	**	**	**	**
10	Cs-137	68766	17505	2362	1062	448	286	183	183	74	22	36	28	16	40
	Bulk Density	0.16	0.23	0.30	0.35	0.31	0.39	0.30	0.47	0.40	0.34	0.43	0.35	0.45	0.26
	Water Content	101.90	100.12	95.99	94.96	93.76	92.61	86.49	84.88	80.95	79.95	81.79	85.63	95.78	92.74
11	Cs-137	232176	104211	31486	11050	2945	1102	551	206	143	79	116	30	22	10
	Bulk Density	0.13	0.18	0.38	0.49	0.47	0.51	0.62	0.61	0.70	0.81	0.72	0.59	0.42	0.66
	Water Content	208.09	142.14	95.80	73.42	60.96	55.51	55.16	45.54	67.48	35.93	32.05	27.73	24.92	24.83
	Sand		72.23				74.11								
	Silt		22.85				22.31								
	Clay		4.92				3.58								
12	Cs-137	133923	84459	17335	8194	3300	3524	2312	704	265	251	164	134	94	68
	Bulk Density	0.17	0.22	0.37	0.44	0.44	0.66	0.52	0.61	0.69	0.68	0.75	0.75	0.65	0.78
	Water Content	142.42	112.92	123.52	61.17	50.75	44.66	41.60	37.45	35.89	34.45	31.76	31.07	30.34	31.03
	Sand	64.59				66.05						71.47			
	Silt	28.66				24.68						24.03			
	Clay	6.74				9.27						4.51			
13	Cs-137	54867	33314	15081	6075	2092	889	428	659	1282	1443	1351	621	1248	867
	Bulk Density	0.36	0.22	0.41	0.38	0.38	0.48	0.42	0.41	0.37	0.51	0.39	0.41	0.32	0.29
	Water Content	92.39	84.10	70.95	65.30	65.52	67.05	69.14	68.69	67.48	68.36	69.98	70.69	68.35	68.83
	Sand					48.22						48.49			
	Silt					42.99						32.01			
	Clay					8.79						19.50			
14	Cs-137	117117	44648	14081	9669	4481	1735	1109	1295	400	169	144	130	71	48
	Bulk Density	0.26	0.23	0.32	0.31	0.41	0.52	0.50	0.44	0.53	0.59	0.50	0.54	0.46	0.42
	Water Content	129.95	102.11	94.46	89.26	82.21	69.11	64.85	67.71	60.60	55.21	53.58	51.44	45.76	39.32
	Sand	43.96					60.07						79.06		
	Silt	26.03					21.23						19.20		
	Clay	30.01					18.70						1.74		
15	Cs-137	66781	3915	949	496	344	124	116	107	29	7	67	12	17	50
	Bulk Density	0.13	0.24	0.30	0.21	0.57	0.43	0.40	0.41	0.42	0.46	0.65	0.44	0.42	0.46
	Water Content	96.51	87.56	81.90	78.57	74.03	61.52	59.77	57.72	45.66	42.75	39.73	37.90	40.58	35.12
16	Cs-137	102253	16905	5694	2148	1151	1046	1142	813	222	80	81	137	67	
	Bulk Density	0.13	0.33	0.14	0.21	0.16	0.20	0.32	0.22	0.23	0.42	0.30	0.31	0.16	
	Water Content	94.75	39.09	83.77	85.35	83.99	82.41	77.02	57.52	52.71	52.60	47.38	49.32	52.58	
17	Cs-137	194963	24305	5319	3184	1314	1602	1278	1160	1123	640	1155	513	276	111
	Bulk Density	0.12	0.18	0.18	0.32	0.32	0.35	0.26	0.25	0.21	0.39	0.32	0.39	0.42	0.36
	Water Content	145.26	109.56	88.23	75.24	66.44	63.52	67.64	66.78	73.94	68.29	70.14	57.35	60.22	54.21
18	Cs-137	441362	43005	5734	2067	1225	826	937	408	378	179	169	380	125	201
	Bulk Density	0.08	0.09	0.25	0.16	0.28	0.20	0.29	0.34	0.31	0.44	0.43	0.46	0.39	0.46
	Water Content	157.09	95.86	84.49	74.53	78.13	76.67	55.61	77.15	69.44	68.94	66.63	62.66	62.50	62.25
19	Cs-137	205075	43467	7656	1580	498	208	115	156	42	53	28	13	10	7
	Bulk Density	0.18	0.17	0.21	0.30	0.27	0.38	0.35	0.36	0.36	0.40	0.42	0.57	0.47	0.45
	Water Content	115.24	126.16	104.24	142.44	90.48	97.83	98.50	88.30	94.63	80.46	70.94	69.74	64.42	68.46

20	Cs-137	229755	73724	21024	19438	2477	807	453	430	60	235	76	33	54	17
	Bulk Density	0.16	0.16	0.25	0.35	0.49	0.36	0.43	0.38	0.32	0.39	0.36	0.09	0.45	0.07
	Water Content	150.79	131.80	110.79	97.05	79.05	71.96	41.52	97.20	86.79	85.14	71.83	**	84.99	**
21	Cs-137	92526	40525	9531	11064	6713	415	265	108	72	71	38	132		
	Bulk Density	0.26	0.34	0.29	0.36	0.51	0.24	0.55	0.55	0.46	0.42	0.34	0.21		
	Water Content	70.08	73.53	66.79	68.47	59.24	231.86	58.26	57.60	56.81	54.06	58.03	62.39		
	Sand		57.51						51.99						
	Silt		33.20						18.88						
	Clay		9.29						29.13						
22	Cs-137	144921	25809	5094	605	364	271	281	244	339	252	130	107	120	115
	Bulk Density	0.23	0.37	0.51	0.56	0.74	0.85	0.79	0.72	0.72	0.87	0.86	0.69	0.70	0.58
	Water Content	196.15	4.61	0.00	31.21	29.49	24.15	21.40	21.80	19.52	16.43	18.24	18.17	19.06	3.10
	Sand		68.45			74.56				86.93					
	Silt		24.49			20.11				11.03					
	Clay		7.06			5.33				2.04					
23	Cs-137	79637	129528	198949	201305	102930	70204	36838	31205						
	Bulk Density	0.23	0.11	0.09	0.15	0.28	0.21	0.31	0.15						
	Water Content	169.42	252.76	311.75	254.41	137.78	150.20	138.81	145.04						
	Sand				58.10										
	Silt				27.35										
	Clay				14.55										
24	Cs-137	42391	7491	2049	495	265	153	158	105	24	24	91	11	27	128
	Bulk Density	0.37	0.53	0.43	0.52	0.50	0.60	0.72	0.76	0.66	0.65	0.68	0.63	0.52	0.67
	Water Content	59.87	59.92	54.61	49.52	44.80	37.79	32.28	28.31	25.47	25.35	28.44	23.89	74.84	21.50
	Sand	51.31							82.76					82.73	
	Silt	38.56							14.59					14.11	
	Clay	10.13							2.65					3.16	
25	Cs-137	380650	23396	5281	1923	525	236	465	295	124	693	63	89	35	59
	Bulk Density	0.20	0.48	0.43	77.90	0.45	0.62	0.60	0.65	0.58	0.64	0.60	0.58	0.47	0.35
	Water Content	74.58	42.40	40.40	15.00	38.50	37.99	36.77	38.01	35.71	38.38	39.00	39.29	38.04	37.01
	Sand			59.79					80.43				68.61		
	Silt			0.96					15.41				23.82		
	Clay			39.25					4.16				7.57		
26	Cs-137	117647	15289	7863	2897	1904	1025	703	466	481	293	114	37	31	42
	Bulk Density	0.26	0.30	0.30	0.32	0.38	0.42	0.48	0.36	0.74	0.50	0.73	0.70	0.62	0.63
	Water Content	81.24	76.79	78.68	74.35	78.78	78.21	71.88	68.02	70.40	58.91	54.95	49.00	46.29	42.83
	Sand			57.60				63.83					65.00		
	Silt			27.29				25.37					27.09		
	Clay			15.11				10.80					7.91		
27	Cs-137	151835	97983	17052	6905	7903	8566	6258	3712	1848	781	975			
	Bulk Density	0.23	0.25	0.48	0.28	0.30	0.27	0.47	0.22	0.29	0.26	0.21			
	Water Content	165.76	144.28	124.83	114.19	135.90	199.70	85.50	210.82	220.38	215.76	220.56			
	Sand		63.94		66.07				57.74						

	Silt		27.67		25.16				32.72						
	Clay		8.39		8.77				9.54						
28	Cs-137	131330	79103	7811	1463	801	369	215	137	204	120	88			
	Bulk Density	0.48	0.36	0.41	0.54	0.45	0.53	0.54	0.70	0.67	0.35	0.32			
	Water Content	40.94	42.19	59.73	63.59	63.06	61.24	58.92	49.60	53.24	50.59	48.83			
	Sand	70.88													
	Silt	21.25													
	Clay	7.87													
29	Cs-137	17349	2193	427	244	182	81	31	41	48	33	66	39	92	25
	Bulk Density	0.78	0.77	0.60	0.79	0.97	1.18	1.06	1.05	0.97	1.31	1.10	1.08	1.08	0.77
	Water Content	57.05	59.81	55.78	56.37	54.64	53.45	51.52	50.89	48.13	51.59	42.52	39.72	38.64	37.85
	Sand			62.36							79.81				
	Silt			27.65							16.49				
	Clay			9.99							3.70				
30	Cs-137	60320	17548	3147	1332	1213	343	523	117	61	83	48	42	70	46
	Bulk Density	0.61	0.56	0.48	0.68	0.92	0.78	0.79	0.64	1.01	1.35	0.96	1.05	0.83	0.51
	Water Content	59.87	33.07	82.06	42.69	42.29	110.23	26.74	40.17	24.16	83.54	40.08	57.22	17.65	38.81
	Sand				57.38							91.74			
	Silt				29.69							7.82			
	Clay				12.93							0.44			
31	Cs-137	43399	18852	11387	9697	9665	3958	661	428	374					
	Bulk Density	0.40	0.51	0.49	0.37	0.49	0.48	0.58	0.52	0.37					
	Water Content	42.56	40.83	40.75	39.79	38.69	37.10	35.01	33.28	30.23					
	Sand			52.54				62.37							
	Silt			37.03				29.22							
	Clay			10.43				8.41							
32	Cs-137	192829	26698	3807	2221	493	31	130	77	45	18				
	Bulk Density	0.16	0.24	0.26	0.35	0.81	0.91	1.01	1.02	1.26	1.43				
	Water Content	371.53	236.85	153.45	136.35	70.90	56.71	54.83	49.28	34.75	23.93				
	Sand		100.00					51.80							
	Silt		0.00					23.15							
	Clay		0.00					25.05							
33	Cs-137	184372	138658	42307	7130	2512	955	636	628	410	288	94	96	50	114
	Bulk Density	0.21	0.24	0.33	0.36	0.41	0.37	0.39	0.42	0.37	0.58	0.49	0.49	0.44	0.39
	Water Content	115.48	107.26	95.32	92.04	95.05	93.55	86.86	82.04	80.32	75.37	68.94	69.33	68.40	69.07
	Sand					52.54						50.77			
	Silt					32.86						35.33			
	Clay					14.60						13.90			
34	Cs-137	438624	87997	12414	5926	2404	2876	1927	915	330	236	190	288	281	62
	Bulk Density	0.16	0.30	0.28	0.25	0.43	0.45	0.39	0.41	0.44	0.51	0.45	0.39	0.34	0.33
	Water Content	132.08	113.62	95.80	84.03	82.84	78.10	76.88	68.84	65.05	63.32	63.86	62.43	69.97	74.17
	Sand		53.34									82.26			
	Silt		37.22									15.23			
	Clay		9.44									2.51			

35	Cs-137	74345	44212	13446	3283	1107	312	206	156	133	48	52	32	41	31
	Bulk Density	0.23	0.26	0.27	0.44	0.28	-	0.37	0.58	0.48	0.36	0.47	0.33	0.21	0.26
	Water Content	87.42	85.83	78.59	80.40	71.12	-	77.83	66.00	65.25	68.53	76.70	86.76	85.03	86.49
	Sand					50.34						45.14			
	Silt					35.26						42.85			
	Clay					14.40						12.01			
36	Cs-137	88597	46131	10591	6805	4295	3074	1694	2265	2206	898	954	374	33	28
	Bulk Density	0.22	0.20	0.37	0.36	0.32	0.31	0.40	0.43	0.47	0.48	0.34	0.46	0.48	0.39
	Water Content	139.62	141.55	129.05	118.82	108.28	99.47	84.03	80.36	82.67	83.96	86.86	89.29	82.52	78.02
	Sand		52.39												
	Silt		36.35												
	Clay		11.26												
37	Cs-137	341424	333968	228288	44244	15697	3111	1180	1302	639	537	634	481	211	210
	Bulk Density	0.17	0.12	0.26	0.40	0.64	0.74	0.59	0.60	0.76	0.88	1.06	0.89	0.86	0.76
	Water Content	204.19	196.33	127.67	61.36	50.88	47.22	43.60	58.34	61.14	35.87	33.83	30.53	25.71	25.52
38	Cs-137	94011	18522	10840	7014	5369	6555	6156	3845	3475	1356	213	319	134	84
	Bulk Density	0.22	0.37	0.27	0.36	0.47	0.30	0.22	0.25	0.31	0.32	0.62	0.42	0.29	0.22
	Water Content	65.09	63.25	55.90	54.03	53.91	52.08	52.49	53.34	53.82	55.52	66.39	65.97	67.38	64.49
	Sand					54.23							61.41		
	Silt					32.36							20.11		
	Clay					13.41							18.48		
39	Cs-137	51130	19659	6515	4091	1252	179	88	119	37	38	45	42	13	
	Bulk Density	0.53	0.46	0.21	0.41	0.41	0.61	0.57	0.60	0.33	0.68	0.32	0.28	0.55	
	Water Content	46.78	68.94	65.65	70.50	70.42	63.14	57.61	55.42	64.95	45.77	38.99	39.54	46.79	
40	Cs-137	21274	9091	6443	1360	557	589	790	587	171	60	49	72	42	
	Bulk Density	0.17	0.26	0.33	0.44	0.46	0.49	0.46	0.52	0.71	0.65	0.58	0.55	0.26	
	Water Content	244.82	138.49	115.71	98.93	88.32	87.47	85.38	79.21	73.57	69.06	66.51	70.77	63.80	
41	Cs-137	420061	117380	52957	12202	1564	1045	925	376	208	179	246	361	273	7197
	Bulk Density	0.16	0.14	0.10	0.39	0.51	0.41	0.46	0.66	0.66	0.67	0.55	0.59	0.61	0.48
	Water Content	136.01	117.24	163.44	70.68	67.94	71.61	68.50	67.77	66.50	61.80	56.87	51.97	53.18	93.25
	Sand		40.98						57.44						
	Silt		43.40						33.58						
	Clay		15.62						8.98						
42	Cs-137	183461	135863	9873	2721	2856	1072	359	243	106	109				
	Bulk Density	0.14	0.29	0.33	0.37	0.42	0.52	0.49	0.61	0.86	0.48				
	Water Content	264.06	95.58	68.36	78.67	97.59	35.77	81.92	106.38	0.00	0.00				
43	Cs-137	155384	96862	17308	3458	608	282	397	696	250	378	251	76	67	119
	Bulk Density	0.11	0.16	0.29	0.31	0.32	0.48	0.46	0.39	0.35	0.50	0.64	0.77	0.38	0.47
	Water Content	111.72	85.64	53.25	43.77	41.13	38.24	34.30	34.02	33.39	33.00	28.35	25.26	25.78	25.18
44	Cs-137	278434	80862	8022	2939	2108	881	596	679	478	309	156	80	110	89
	Bulk Density	0.09	0.07	0.36	0.34	0.37	0.31	0.30	0.32	0.46	0.46	0.54	0.44	0.31	0.34
	Water Content	200.90	142.59	57.96	50.04	51.66	53.46	47.41	50.26	46.57	42.93	42.64	43.58	43.45	41.40
45	Cs-137	127903	146942	76726	11306	2174	1209	893	837	1399	1366	492	237	246	48
	Bulk Density	0.17	0.21	0.29	0.39	0.48	0.47	0.51	0.54	0.51	0.55	0.70	0.64	0.81	0.66

	Water Content	138.62	99.17	98.40	79.85	48.55	49.93	50.12	51.58	50.01	47.77	41.88	39.33	18.83	31.59
46	Cs-137	132663	114603	73679	65386	57707	14840	31403	37959	10267	3781	1262	419	174	171
	Bulk Density	0.37	0.41	0.34	0.39	0.43	0.35	0.29	0.29	0.29	0.44	0.52	0.36	0.41	0.38
	Water Content	194.79	194.88	213.01	206.12	186.15	194.34	230.21	235.30	192.41	123.60	133.76	215.32	199.56	120.96
	Sand			91.51							74.70				
	Silt			8.41							18.19				
	Clay			0.08							7.11				

***rock fragment**

****not included due to an inaccurate measurement of soil volume**

References

Amaral, E., Amundsen, I., Barišić, D., Booth, P., Clark, D., Ditmars, J., Dlouhy, Z., Drury, N., Gehrche, K. and Gnugnoli, G.: Characterization of radioactively contaminated sites for remediation purposes, IAEA-Tecdoc, 1017, 1-103, 1998.

Bennett, S. J., Rhoton, F. E. and Dunbar, J. A.: Texture, spatial distribution, and rate of reservoir sedimentation within a highly erosive, cultivated watershed: Grenada Lake, Mississippi, Water resources research, 41, 1, doi:10.1029/2004wr003645, 2005.

Bivand, R. S., Pebesma, E. J., Gómez-Rubio, V. and Pebesma, E. J.: Applied spatial data analysis with R, Springer, 2008.

Burr, T. and Hamada, M.: Radio-Isotope Identification Algorithms for NaI γ Spectra, Algorithms, 2, 1, 339-360, doi:10.3390/a2010339, 2009.

Catani, F., Segoni, S. and Falorni, G.: An empirical geomorphology-based approach to the spatial prediction of soil thickness at catchment scale, Water Resources Research, 46, 5, doi:10.1029/2008wr007450, 2010.

Chen, Z.-S., Hsieh, C.-F., Jiang, F.-Y., Hsieh, T.-H. and Sun, I.-F.: Relations of soil properties to topography and vegetation in a subtropical rain forest in southern Taiwan, Plant Ecology, 132, 2, 229-241, doi:10.1023/A:1009762704553, 1997.

Claessens, L., Heuvelink, G., Schoorl, J. and Veldkamp, A.: DEM resolution effects on shallow landslide hazard and soil redistribution modelling, Earth Surface Processes and Landforms: The Journal of the British Geomorphological Research Group, 30, 4, 461-477, 2005.

Clark, M.: Generalized additive models: getting started with additive models in R, Center for Social Research, University of Notre Dame, 35, 2013.

Claverie, M., Garcia, J., Prevost, T., Brendlé, J. and Limousy, L.: Inorganic and Hybrid (Organic–Inorganic) Lamellar Materials for Heavy Metals and Radionuclides Capture in Energy Wastes Management—A Review, Materials, 12, 9, 1399, doi:10.3390/ma12091399, 2019.

Climate-Data.Org: Prypiat Climate https://en.climate-data.org/europe/ukraine/kyiv-oblast/prypiat-715182/, Last Accessed: Nov 25, 2019.

Cook, R. D.: Detection of influential observation in linear regression, Technometrics, 19, 1, 15-18, doi:10.2307/1268249, 1977.

Doerr, H. and Münnich, K.: Downward movement of soil organic matter and its influence on trace-element transport (210Pb, 137Cs) in the soil, Radiocarbon, 31, 3, 655-663, doi:10.1017/s003382220001225x, 1989.

Dumat, C., Cheshire, M., Fraser, A., Shand, C. and Staunton, S.: The effect of removal of soil organic matter and iron on the adsorption of radiocaesium, European Journal of Soil Science, 48, 4, 675-683, doi:10.1111/j.1365-2389.1997.tb00567.x, 1997.

Dumat, C., Quiquampoix, H. and Staunton, S.: Adsorption of cesium by synthetic clay− organic matter complexes: effect of the nature of organic polymers, Environmental science & technology, 34, 14, 2985-2989, doi:10.1021/es990657o, 2000.

Eguchi, S., Aoki, K. and Kohyama, K.: Development of agricultural soil-profile physical properties database, Japan: SolphyJ,Proceedings of the ASA-CSSA-SSSA International Annual Meetings, San Antonio, TX, USA, 2011, 16-19

EPA: Radiological Laboratory Sample Analysis Guide for Incident Response – Radionuclides in Soil, 2012.

EPA: PAG Manual: Protective Action Guides and Planning Guidance for Radiological Incidents, 2017.

Fan, Q., Tanaka, M., Tanaka, K., Sakaguchi, A. and Takahashi, Y.: An EXAFS study on the effects of natural organic matter and the expandability of clay minerals on cesium adsorption and mobility, Geochimica et Cosmochimica Acta, 135, 49-65, doi:10.1016/j.gca.2014.02.049, 2014.

Friedman, J. H. and Stuetzle, W.: Projection pursuit regression, Journal of the American statistical Association, 76, 376, 817-823, 1981.

Fujii, K., Ikeda, S., Akama, A., Komatsu, M., Takahashi, M. and Kaneko, S.: Vertical migration of radiocesium and clay mineral composition in five forest soils contaminated by the Fukushima nuclear accident, Soil science and plant nutrition, 60, 6, 751-764, doi:10.1080/00380768.2014.926781, 2014.

Fukushima Prefecture: ふくしま森林文化企画展図録, 2010.

Gallant, J. C. and Wilson, J. P.: TAPES-G: a grid-based terrain analysis program for the environmental sciences, Computers & Geosciences, 22, 7, 713-722, doi:10.1016/0098-3004(96)00002-7, 1996.

Gessler, P. E., Moore, I., McKenzie, N. and Ryan, P.: Soil-landscape modelling and spatial prediction of soil attributes, International Journal of Geographical Information Systems, 9, 4, 421-432, doi:10.1080/02693799508902047, 1995.

Griffiths, R. P., Madritch, M. D. and Swanson, A. K.: The effects of topography on forest soil characteristics in the Oregon Cascade Mountains (USA): Implications for the effects of climate change on soil properties, Forest Ecology and Management, 257, 1, 1-7, doi:10.1016/j.foreco.2008.08.010, 2009.

Hastie, T., Tibshirani, R. and Friedman, J.: The elements of statistical learning: data mining, inference, and prediction, Springer Science & Business Media, 2009.

Hastie, T. J. and Tibshirani, R. J.: Generalized additive models, CRC press, 1990.

Heimsath, A., Dietrich, W., Nishiizumi, K. and Finkel, R.: The soil production function and landscape equilibrium, Nature, 388, 6640, 358, doi:10.1038/41056, 1997.

Heimsath, A. M., Dietrich, W. E., Nishiizumi, K. and Finkel, R. C.: Cosmogenic nuclides, topography, and the spatial variation of soil depth, Geomorphology, 27, 1-2, 151-172, doi:10.1016/s0169-555x(98)00095-6, 1999.

Hengl, T. and Reuter, H. I.: Geomorphometry: concepts, software, applications, Newnes, 2008.

Hoover, M. and Hursh, C.: Influence of topography and soil-depth on runoff from forest land, Eos, Transactions American Geophysical Union, 24, 2, 693-698, doi:10.1029/tr024i002p00693, 1943.

IAEA-TECDOC: Manual for reactor produced radioisotopes, Vienna: International Atomic Energy Agency, 2003.

IAEA: Fukushima Daiichi Accident Technical Volume 4/5 Radiological Consequences, 2015.

IAEA and INES: The international nuclear and radiological event scale, Information Series, International Atomic Energy Agency, Vienna, Austria, 4, 2008.

Ivanov, Y. A., Lewyckyj, N., Levchuk, S., Prister, B., Firsakova, S., Arkhipov, N., Arkhipov, A., Kruglov, S., Alexakhin, R. and Sandalls, J.: Migration of 137Cs and 90Sr from Chernobyl fallout in Ukrainian, Belarussian and Russian soils, Journal of Environmental Radioactivity, 35, 1, 1-21, doi:10.1016/s0265-931x(96)00036-7, 1997.

Iwagami, S., Tsujimura, M., Onda, Y., Nishino, M., Konuma, R., Abe, Y., Hada, M., Pun, I., Sakaguchi, A. and Kondo, H.: Temporal changes in dissolved 137 Cs concentrations in groundwater and stream water in Fukushima after the Fukushima Dai-ichi Nuclear Power Plant accident, Journal of environmental radioactivity, doi:10.1016/j.jenvrad.2015.03.025, 2015.

Japan Meteorological Agency: Data and References, http://www.jma.go.jp/jma/menu/menureport.html, Last Accessed: September 2, 2019.

Kato, H., Onda, Y. and Teramage, M.: Depth distribution of 137 Cs, 134 Cs, and 131 I in soil profile after Fukushima Dai-ichi Nuclear Power Plant accident, Journal of Environmental Radioactivity, 111, 59-64, doi:10.1016/j.jenvrad.2011.10.003, 2012.

Kim, S. and Lee, H.: A digital elevation analysis: a spatially distributed flow apportioning algorithm, Hydrological Processes, 18, 10, 1777-1794, doi:10.1002/hyp.1446, 2004.

Koarashi, J., Atarashi-Andoh, M., Matsunaga, T., Sato, T., Nagao, S. and Nagai, H.: Factors affecting vertical distribution of Fukushima accident-derived radiocesium in soil under different land-use conditions, Science of the Total Environment, 431, 392-401, doi:10.1016/j.scitotenv.2012.05.041, 2012.

Komamura, M., Tsumura, A., Yamaguchi, N., Fujiwara, E., Konokata, N. and Kodaira, K.: わが国の米, 小麦および土壌における 90Sr と 137Cs 濃度の長期モニタリングと変動解析, 農業環境技術研究所報告, 24, 1-21, 2006.

Komissarov, M. and Ogura, S.: Distribution and migration of radiocesium in sloping landscapes three years after the Fukushima-1 nuclear accident, Eurasian Soil Science, 50, 7, 861-871, doi:10.1134/s1064229317070043, 2017.

Korobova, E. M., Linnik, V. G. and Brown, J.: Distribution of artificial radioisotopes in granulometric and organic fractions of alluvial soils downstream from the Krasnoyarsk Mining and Chemical Combine (KMCC), Russia, Journal of soils and sediments, 16, 4, 1279-1287, doi:10.1007/s11368-015-1268-2, 2016.

Linnik, V. G., Saveliev, A. A. and Sokolov, A. V.: Transformation of the Chernobyl 137 Cs Contamination Patterns at the Microlandscape Level as an Indicator of Stochastic Landscape Organization, Landscape Patterns in a Range of Spatio-Temporal Scales, Springer, 77-89,2020.

Loughran, R., Campbell, B. and Walling, D.: Soil erosion and sedimentation indicated by caesium 137: Jackmoor Brook catchment, Devon, England, Catena, 14, 1-3, 201-212, doi:10.1016/s0341-8162(87)80018-8, 1987.

Lowrance, R., McIntyre, S. and Lance, C.: Erosion and deposition in a field/forest system estimated using cesium-137 activity, Journal of soil and water conservation, 43, 2, 195-199, 1988.

Mabit, L., Bernard, C. and Laverdière, M. R.: Assessment of erosion in the Boyer River watershed (Canada) using a GIS oriented sampling strategy and 137Cs measurements, Catena, 71, 2, 242-249, doi:10.1016/j.catena.2006.02.011, 2007.

Mabit, L., Bernard, C., Makhlouf, M. and Laverdière, M.: Spatial variability of erosion and soil organic matter content estimated from 137Cs measurements and geostatistics, Geoderma, 145, 3-4, 245-251, doi:10.1016/j.geoderma.2008.03.013, 2008.

Mahaffey, J.: Atomic Accidents: A History of Nuclear Meltdowns and Disasters: from the Ozark Mountains to Fukushima, Open Road Media, 2014.

Martin-Garin, A., Van Meir, N., Simonucci, C., Kashparov, V. and Bugai, D.: Quantitative assessment of radionuclide migration from near-surface radioactive waste burial sites: the waste dumps in the Chernobyl exclusion zone as an example, Radionuclide Behaviour in the Natural Environment, Elsevier, 570-600,2012.

Martin, Y.: Modelling hillslope evolution: linear and nonlinear transport relations, Geomorphology, 34, 1-2, 1-21, doi:10.1016/s0169-555x(99)00127-0, 2000.

Martinez, C., Hancock, G., Kalma, J., Wells, T. and Boland, L.: An assessment of digital elevation models and their ability to capture geomorphic and hydrologic properties at the catchment scale, International Journal of Remote Sensing, 31, 23, 6239-6257, 2010.

Martz, L. and De Jong, E.: Using Cesium-137 to assess the variability of net soil erosion and its association with topography in a Canadian prairie landscape, Catena, 14, 5, 439-451, doi:10.1016/0341-8162(87)90014-2, 1987.

Matsunaga, T., Koarashi, J., Atarashi-Andoh, M., Nagao, S., Sato, T. and Nagai, H.: Comparison of the vertical distributions of Fukushima nuclear accident radiocesium in soil before and after the first rainy season, with physicochemical and mineralogical interpretations, Science of the total environment, 447, 301-314, doi:10.1016/j.scitotenv.2012.12.087, 2013.

MEXT, J.: 第 48 回環境放射能調査研究 成果論文抄録集, Ministry of Education, Culture, Sports, Science and Technology, Japan, 2006.

MEXT, J.: 文部科学省による放射線量等分布マップ (放射性セシウムの土壌濃度マップ) の作成について, http://radioactivity. mext. go. jp/ja/ontents/6000/5043/24/11555_0830. pdf, 2011.

Miller, B. A., Koszinski, S., Wehrhan, M. and Sommer, M.: Impact of multi-scale predictor selection for modeling soil properties, Geoderma, 239, 97-106, 2015.

Miyahara, K. A., T; Kohara, Y; Yusa, Y; Sasaki, N: Effect of bulk density on diffusion for cesium in compacted sodium bentonite, Radiochimica Acta, 52, 2, 293-298, doi:10.1524/ract.1991.5253.2.293, 1991.

Momm, H. G., Bingner, R. L., Wells, R. R. and Wilcox, D.: AGNPS GIS-based tool for watershed-scale identification and mapping of cropland potential ephemeral gullies, Applied engineering in agriculture, 28, 1, 17-29, doi:10.13031/2013.41282, 2012.

Moore, I. D., Gessler, P., Nielsen, G. and Peterson, G.: Soil attribute prediction using terrain analysis, Soil Science Society of America Journal, 57, 2, 443-452, doi:10.2136/sssaj1993.03615995005700020026x, 1993.

Murota, K., Saito, T. and Tanaka, S.: Desorption kinetics of cesium from Fukushima soils, Journal of environmental radioactivity, 153, 134-140, doi:10.1016/j.jenvrad.2015.12.013, 2016.

Nagao, S.: Radionuclides released from nuclear accidents: Distribution and dynamics in soil, Environmental Remediation Technologies for Metal-Contaminated Soils, Springer, 43-65,2016.

Nakao, A., Thiry, Y., Funakawa, S. and Kosaki, T.: Characterization of the frayed edge site of micaceous minerals in soil clays influenced by different pedogenetic conditions in Japan and northern Thailand, Soil science and plant nutrition, 54, 4, 479-489, doi:10.1111/j.1747-0765.2008.00262.x, 2008.

Nobori, T., Tanoi, K. and Nakanishi, T.: オートサンプラー付き NaI (Tl) シンチレーションカウンターによる土壌および作物中の放射性セシウム測定, Japanese Journal of Soil Science and Plant Nutrition, 84, 3, 182-186, 2013.

Ohnuki, T. and Kozai, N.: Adsorption behavior of radioactive cesium by non-mica minerals, Journal of Nuclear Science and Technology, 50, 4, 369-375, doi:10.1080/00223131.2013.773164, 2013.

Onda, Y., Kato, H., Hoshi, M., Takahashi, Y. and Nguyen, M.-L.: Soil sampling and analytical strategies for mapping fallout in nuclear emergencies based on the Fukushima Dai-ichi Nuclear Power Plant accident, Journal of environmental radioactivity, 139, 300-307, doi:10.1016/j.jenvrad.2014.06.002 2015.

Osawa, K., Nonaka, Y., Nishimura, T., Tanoi, K., Matsui, H., Mizogichi, M. and Tatsuno, T.: Quantification of dissolved and particulate radiocesium fluxes in two rivers draining the main radioactive pollution plume in Fukushima, Japan (2013–2016), Anthropocene, 22, 40-50, doi:10.1016/j.ancene.2018.04.003, 2018.

Park, S.-M., Alessi, D. S. and Baek, K.: Selective adsorption and irreversible fixation behavior of cesium onto 2: 1 layered clay mineral: A mini review, Journal of hazardous materials, 369, 569-576, doi:10.1016/j.jhazmat.2019.02.061, 2019.

Pennock, D., Jong, E. d. and Lemmen, D.: Cesium-137-measured erosion rates for soils of five parent-material groups in southwestern Saskatchewan, Canadian Journal of Soil Science, 75, 2, 205-210, doi:10.4141/cjss95-028, 1995.

Quine, T. A., Govers, G., Walling, D. E., Zhang, X., Desmet, P. J., Zhang, Y. and Vandaele, K.: Erosion processes and landform evolution on agricultural land—new perspectives from caesium-137 measurements and topographic-based erosion modelling, Earth Surface Processes and Landforms: The Journal of the British Geomorphological Group, 22, 9, 799-816, doi:10.1002/(sici)1096-9837(199709)22:9<799::aid-esp765>3.0.co;2-r, 1997.

Quinn, P., Beven, K., Chevallier, P. and Planchon, O.: The prediction of hillslope flow paths for distributed hydrological modelling using digital terrain models, Hydrological processes, 5, 1, 59-79, doi:10.1002/hyp.3360050106, 1991.

Quinn, P., Beven, K. and Lamb, R.: The in (a/tan/β) index: How to calculate it and how to use it within the topmodel framework, Hydrological processes, 9, 2, 161-182, doi:10.1002/hyp.3360090204, 1995.

R Core Team: R Foundation for Statistical Computing; Vienna, Austria: 2014, R: A language and environment for statistical computing, 2013, 2015.

Ritchie, J. and Ritchie, C.: 137 Cs use in erosion and sediment deposition studies: Promises and problems, 1995.

Ritchie, J. C. and McHenry, J. R.: Application of radioactive fallout cesium-137 for measuring soil erosion and sediment accumulation rates and patterns: a review, Journal of environmental quality, 19, 2, 215-233, doi:10.2134/jeq1990.00472425001900020006x, 1990.

Roering, J., Kirchner, J. and Dietrich, W.: Hillslope evolution by nonlinear, slope-dependent transport: Steady state morphology and equilibrium adjustment timescales, Journal of Geophysical Research: Solid Earth, 106, B8, 16499-16513, doi:10.1029/2001jb000323 2001.

Roering, J. J.: How well can hillslope evolution models "explain" topography? Simulating soil transport and production with high-resolution topographic data, Geological Society of America Bulletin, 120, 9-10, 1248-1262, doi:10.1130/B26283.1, 2008.

Roering, J. J., Kirchner, J. W. and Dietrich, W. E.: Evidence for nonlinear, diffusive sediment transport on hillslopes and implications for landscape morphology, Water Resources Research, 35, 3, 853-870, doi:10.1029/1998wr900090, 1999.

Rosén, K., Öborn, I. and Lönsjö, H.: Migration of radiocaesium in Swedish soil profiles after the Chernobyl accident, 1987–1995, Journal of Environmental Radioactivity, 46, 1, 45-66, doi:10.1016/s0265-931x(99)00040-5, 1999.

Rossi, G., Ferrarini, A., Dowgiallo, G., Carton, A., Gentili, R. and Tomaselli, M.: Detecting complex relations among vegetation, soil and geomorphology. An in-depth method applied to a case study in the Apennines (Italy), Ecological Complexity, 17, 87-98, doi:10.1016/j.ecocom.2013.11.002, 2014.

Sakuma, K., Tsuji, H., Hayashi, S., Funaki, H., Malins, A., Yoshimura, K., Kurikami, H., Kitamura, A., Iijima, K. and Hosomi, M.: Applicability of Kd for modelling dissolved 137Cs concentrations in Fukushima river water: Case study of the upstream Ota River, Journal of environmental radioactivity, 184, 53-62, doi:10.1016/j.jenvrad.2018.01.001, 2018.

Schimmack, W., Bunzl, K., Dietl, F. and Klotz, D.: Infiltration of radionuclides with low mobility (137Cs and 60Co) into a forest soil. Effect of the irrigation intensity, Journal of environmental radioactivity, 24, 1, 53-63, doi:10.1016/0265-931x(94)90024-8 1994.

Schimmack, W., Bunzl, K. and Zelles, L.: Initial rates of migration of radionuclides from the Chernobyl fallout in undisturbed soils, Geoderma, 44, 2-3, 211-218, doi:10.1016/0016-7061(89)90030-x 1989.

Sørensen, R. and Seibert, J.: Effects of DEM resolution on the calculation of topographical indices: TWI and its components, Journal of Hydrology, 347, 1-2, 79-89, 2007.

Staunton, S., Dumat, C. and Zsolnay, A.: Possible role of organic matter in radiocaesium adsorption in soils, Journal of Environmental Radioactivity, 58, 2, 163-173, doi:10.1016/s0265-931x(01)00064-9 2002.

Stevens, J. P.: Outliers and influential data points in regression analysis, Psychological Bulletin, 95, 2, 342, 1984.

Stinnett, J. and Sullivan, C. J.: An automated isotope identification algorithm using Bayesian statistics,2013 IEEE Nuclear Science Symposium and Medical Imaging Conference (2013 NSS/MIC), 2013, IEEE, 1-7

Takahashi, J., Tamura, K., Suda, T., Matsumura, R. and Onda, Y.: Vertical distribution and temporal changes of 137Cs in soil profiles under various land uses after the Fukushima Dai-ichi Nuclear Power Plant accident, Journal of environmental radioactivity, 139, 351-361, doi:10.1016/j.jenvrad.2014.07.004 2015.

Takenaka, C., Onda, Y. and Hamajima, Y.: Distribution of cesium-137 in Japanese forest soils: Correlation with the contents of organic carbon, Science of the total environment, 222, 3, 193-199, doi:10.1016/s0048-9697(98)00305-2, 1998.

Tanaka, K., Takahashi, Y., Sakaguchi, A., Umeo, M., Hayakawa, S., Tanida, H., Saito, T. and Kanai, Y.: Vertical profiles of iodine-131 and cesium-137 in soils in Fukushima prefecture related to the Fukushima Daiichi Nuclear Power Station accident, Geochemical Journal, 46, 1, 73-76, doi:10.2343/geochemj.1.0137, 2012.

Tanoi, K., Nobori, T., Shiomi, S., Saito, T., Kobayashi, N. I., Leonhardt, N. and Nakanishi, T. M.: Chapter 3 Cesium Translocation in Rice, Agricultural Implications of the Fukushima Nuclear Accident (III), Springer, 15-25,2019.

Tarboton, D. G.: A new method for the determination of flow directions and upslope areas in grid digital elevation models, Water resources research, 33, 2, 309-319, doi:10.1029/96wr03137, 1997.

Tatsuno, T., Hamamoto, S., Nihei, N. and Nishimura, T.: Effects of the dissolved organic matter on Cs transport in the weathered granite soil, Journal of environmental management, 254, 109785, doi:10.1016/j.jenvman.2019.109785 2020.

Teramage, M. T., Onda, Y., Patin, J., Kato, H., Gomi, T. and Nam, S.: Vertical distribution of radiocesium in coniferous forest soil after the Fukushima nuclear power plant accident, Journal of environmental radioactivity, 137, 37-45, doi:10.1016/j.jenvrad.2014.06.017, 2014.

Tesfa, T. K., Tarboton, D. G., Chandler, D. G. and McNamara, J. P.: Modeling soil depth from topographic and land cover attributes, Water Resources Research, 45, 10, doi:10.1029/2008wr007474, 2009.

Tsoulfanidis, N.: Nuclear energy: selected entries from the encyclopedia of sustainability science and technology, Springer Science & Business Media, 2012.

Tsuji, H., Nishikiori, T., Yasutaka, T., Watanabe, M., Ito, S. and Hayashi, S.: Behavior of dissolved radiocesium in river water in a forested watershed in Fukushima Prefecture, Journal of Geophysical Research: Biogeosciences, 121, 10, 2588-2599, doi:10.1002/2016jg003428, 2016.

Tsukada, H., Hasegawa, H., Hisamatsu, S. i. and Yamasaki, S. i.: Transfer of 137 Cs and stable Cs from paddy soil to polished rice in Aomori, Japan, Journal of environmental radioactivity, 59, 3, 351-363, doi:10.1016/s0265-931x(01)00083-2, 2002.

US EPA: Radionuclide Basics: Cesium-137, Radiation Protection, https://www.epa.gov/radiation/radionuclide-basics-cesium-137, Last Accessed: Aug 22, 2017.

Wallbrink, P., Roddy, B. and Olley, J.: A tracer budget quantifying soil redistribution on hillslopes after forest harvesting, Catena, 47, 3, 179-201, doi:10.1016/s0341-8162(01)00185-0, 2002.

Walling, D. and He, Q.: Models for converting 137Cs measurements to estimates of soil redistribution rates on cultivated and uncultivated soils (including software for model implementation), Report to IAEA, University of Exeter, UK, 315-341, 1997.

Walling, D., He, Q. and Quine, T.: Use of caesium-137 and lead-210 as tracers in soil erosion investigations, IAHS Publications-Series of Proceedings and Reports-Intern Assoc Hydrological Sciences, 229, 163-172, 1995.

Walling, D., Zhang, Y. and He, Q.: Models for converting measurements of environmental radionuclide inventories (137Cs, Excess 210Pb, and 7Be) to estimates of soil erosion and deposition rates (including software for model implementation), Department of Geography, University of Exeter, UK, 2007.

Wood, S. N.: Generalized additive models: an introduction with R, Chapman and Hall/CRC, 2017.

Wood, S. N., Pya, N. and Säfken, B.: Smoothing parameter and model selection for general smooth models, Journal of the American Statistical Association, 111, 516, 1548-1563, 2016.

Wrixon, A. D., I. Barraclough, and M. J. Clark: RADIATION, PEOPLE AND THE ENVIRONMENT, 2004.

Xinbao, Z., Higgitt, D. and Walling, D.: A preliminary assessment of the potential for using caesium-137 to estimate rates of soil erosion in the Loess Plateau of China, Hydrological Sciences Journal, 35, 3, 243-252, doi:10.1080/02626669009492427, 1990.

Yang, C., Peterson, C., Shropshire, G. and Otawa, T.: Spatial variability of field topography and wheat yield in the palouse region of the Pacific Northwest, Transactions of the ASAE, 41, 1, 17, doi:10.13031/2013.17147, 1998.

Zaslavsky, D. and Sinai, G.: Surface hydrology: I—explanation of phenomena, Journal of the Hydraulics Division, 107, 1, 1-16, 1981.

Table 1. Soil sampling projects conducted in the Fukushima region following the 2011 FDNPP accident (through 2019).

Authors	Publication year	Sampling year	Land use type	Soil collection methods	Greatest sample depth (cm)
Shiozawa et al.	2011	2011	Rice paddies	Scoop and cylinder	15
Tagami et al.	2011	2011	Flower garden	Scoop	12
Tanaka et al.	2012	2011	Field, orchard	Stainless steel pipe	30
Fujiwara et al.	2012	2011	Forest, rice paddy, urban	House-made soil sampler	30
Koarashi et al.	2012	2011	Croplands, grasslands, pastures	Core sampling technique	20
Kato et al.	2012	2011	Home garden at a residence	Scraper plate	30
Ohno et al.	2012	2011	Wheatfields, rice paddies, orchards, and forestland	A stainless steel core sampler	20
Endo et al.	2012	2011	Uncultivated lands, such as shrubs, school playgrounds, flowerbeds, and a sandbox (in a park)	NA	10
Yamamoto et al.	2012	2011	Roadside, school playgrounds and paddy or dry fields	Stainless steel pipe, soil sampler	30
Taira et al.	2012	2011	Undisturbed surface soils	Core sampling	10
Zheng et al.	2012	2011	Research center ground, public park, garden, forest	NA	13
Endo et al.	2013	2011	Rice paddy fields	NA	30
Nakanishi et al.	2013	2011	General farming field, vegetable field, wheat field, paddy soil field for rice	NA	NA
Matsunaga et al.	2013	2011	Croplands, grasslands, forests	Core sampler	25
Tanaka et al.	2013	2012	Paddy field	Plastic corer, stainless steel pipe equipped with an inner plastic corer	30
Saito et al.	2014	2011	NA	House-made soil sampler	5
Takata et al.	2014	2011-12	Upland, paddy fields, orchard, meadow	Hand sampler	15
Sakai et al.	2014	2011-12	Rice paddies	NA	20
Nakanishi et al.	2014	2011-12	Forest	NA	10
Fujii et al.	2014	2011–12	Forest	Core sampler	20
Yoshikawa et al.	2014	2012	Paddy field	Soil sampler	15
Takahashi et al.	2015	2011–12	Forests, pasture, meadow, farmland, tobacco field, rice paddy	Scraper plate	10
Maekawa et al.	2015	2011–12	NA	Stainless steel tube	15
Matsuda et al.	2015	2011–12	NA	Scraper plate	8
Saito et al.	2015	2011	Fields with little vegetation (farm fields were avoided)	See Onda, et al., (2015)	5
Lepage et al.	2015	2013	Paddy fields	Augur	20
Onda et al.	2015	2011	Forest floor, grassland, and paddy field	Plastic container, core sampler	5

Yang et al.	2016	2011–14	Rice paddies	See Onda, et al., (2015)	30
Ayabe et al.	2017	2013–15	Secondary forests	NA	5
Wakai et al.	2019	2014	Roadside, paddy, upland, canal ditch, mountain	Soil sampling scoop	5

Table 2. A comparison of climates, topographies, and soil formations between the FDNPP accident–affected area and the CNPP accident–affected area.

Attribute	FDNPP accident–affected area	CNPP accident–affected area
Climate	Humid; Cfa (Köppen climate system)	Warm-summer humid continental climate; Dfb (Köppen)
Average annual precipitation	1362 mm (Japan Meteorological Agency, 2019)	621 mm (Climate-Data.Org, 2019).
Topography and vegetation cover	Mountainous with forests (deciduous and evergreen trees)	Steppes and plateaus
Natural soil transformation	Volcanic activity, weathering	Glacial activity, weathering

Table 3. Background levels of Cs-137 in soils in Japan before the FDNPP accident (the highest concentration at a measured soil depth).

Location	Sample year	Highest concentration	Measured depth (cm)
Ibaragi, 180 km southwest of FDNPP (Yamaguchi, et al., 2012)	1996	50 Bq kg^{-1} (forest)	10
Sea of Japan side (Komamura, et al., 2006)	1959–1978	100 Bq kg^{-1} (rice paddy)	NA
Aomori, 350 km north of FDNPP (Tsukada, et al., 2002)	1996—1997	15 Bq kg^{-1} (paddy soil)	5–20
Fukushima City, 60 km northwest of FDNPP (MEXT, 2006)	2005	21 Bq kg^{-1}	0–5

Table 4. The results of single topographic parameter GAMs for deviance explained percentages and the number of depth layers where p-values were equal to or less than 0.05. "( )" indicates standard deviation.

		1 m DEM		
Parameter	**Deviance explained (%)**	**# of layers with p≤0.05**	**Deviance explained (%)**	**# of layers with p≤0.05**
	Bq kg^{-1}		**Bq m^{-2}**	
elevation (m)	20.63 (14.49)	1/14	19.59 (13.06)	2/14
upslope distance (m)	13.32 (14.41)	0/14	8.65 (13.24)	0/14
slope (degrees)	18.78 (22.76)	1/14	8.94 (18.34)	1/14
plan curvature	17.22 (14.63)	2/14	16.23 (11.85)	0/14
TWI	27.35 (20.78)	2/14	22.70 (18.04)	3/14
		10 m DEM		
Parameter	**Deviance explained (%)**	**# of layers with p≤ 0.05**	**Deviance explained (%)**	**# of layers with p≤ 0.05**
	Bq kg^{-1}	**Bq m^{-2}**	**Bq kg^{-1}**	**Bq m^{-2}**
elevation (m)	22.18 (13.28)	0/14	19.24 (11.55)	014
upslope distance (m)	22.69 (17.26)	3/14	18.16 (17.64)	2/14
slope (degrees)	28.31 (18.36)	7/14	22.38 (17.55)	6/14
plan curvature	3.83 (5.26)	0/14	4.95 (7.98)	0/14
TWI	27.64 (17.92)	1/14	22.80 (20.83)	1/14

Table 5. The results of single soil property parameter GAMs for deviance explained and the number of depth layers where p-values were equal to or less than 0.05. "( )" indicates standard deviation.

Parameter	**Deviance explained (%)**	**# of layers with p≤0.05**	**Deviance explained (%)**	**# of layers with p≤0.05**
	Bq kg^{-1}		**Bq m^{-2}**	
water content (%)	36.16 (20.21)	12/14	27.75 (24.60)	8/14
bulk density (g cm^{-3})	31.79 (17.02)	10/14	17.93 (16.83)	5/14

Table 6. The most effective parameter combinations with the best deviance-explained percentages and the number of depth layers where p-values were equal to or less than 0.05. "( )" indicates standard deviation. The two models [A] and [B] in bold were used for reverse prediction accuracy checks.

1 m DEM							
Parameter combinations		Core average deviance explained (%)	# of layers with p≤0.05	Parameter combinations		Core average deviance explained (%)	# of layers with p≤0.05
Bq kg^{-1}				Bq m^{-2}			
All	water content + bulk density + elevation	53.56 (20.00)	5/14	All	water content + bulk density + elevation	43.58 (23.94)	5/14
Topo* only	slope + plan curvature + TWI	40.62 (26.05)	0/14	Topo only	elevation + plan curvature + TWI	37.89 (23.40)	0/14
10 m DEM							
Parameter combinations		**Core average deviance explained (%)**	**# of layers with p≤0.05**	**Parameter combinations**		**Core average deviance explained (%)**	**# of layers with p≤ 0.05**
Bq kg^{-1}				**Bq m^{-2}**			
All [Model A]	**water content + bulk density + elevation**	**54.03 (19.06)**	**6/14**	All	water content + bulk density + elevation	44.09 (23.40)	4/14
Topo only [Model B]	**elevation + slope + upslope distance**	**46.70 (26.02)**	**4/14**	Topo only	elevation + slope + upslope distance	41.83 (26.54)	4/14

*An abbreviation of "Topography."

Table 7. Comparison of Cs-137 downward migration depth between the CNPP accident–affected area and Fukushima at about the same length of time after the nuclear plant accidents.

Ukraine, Belarus, Russia (Ivanov et al., 1997; 15 samples)			Current Study (Iitate Village, Fukushima, Japan; 58 samples)			
Depth (cm) of 90% threshold of Cs-137 accumulation (Bq m^{-2})	Number and % of samples		Depth (cm) of 90% threshold of Cs-137 accumulation (Bq m^{-2})	Number and % of samples		
	Years passed 7	Years passed 8		Years passed 6	Years passed 7	Years passed 8
2	1 (6.7%)	1 (6.7%)	2			
4	6 (40.0%)	1 (6.7%)	4	8 (13.8%)	1 (1.7%)	10 (17.2%)
6	1 (6.7%)	1 (6.7%)	6	5 (8.6%)		5 (8.6%)
7	3 (20.0%)		7			
			8	5 (8.6%)	3 (5.2%)	6 (10.3%)
10		1 (6.7%)	10	2 (3.4%)	1 (1.7%)	3 (5.2%)
			12	2 (3.4%)	1 (1.7%)	4 (6.9%)
			18			1 (1.7%)
			20		1 (1.7%)	

Table 8. Topographic value difference ratio between the 1 m and 10 m resolution DEMs (medians). The right column shows with which DEM, 1 m or 10 m, each topographic parameter appeared in the best performing model.

Difference ratio	1 m DEM	10 m DEM	The DEM where each parameter appeared in the better-performing models
elevation	1.00	1.01	1 m / 10 m DEM
slope	1.08	1.00	1 m / 10 m DEM
upslope distance	1.00	4.05	10 m DEM
plan curvature	1.00	3.33	1 m DEM
TWI	1.00	3.34	1 m DEM

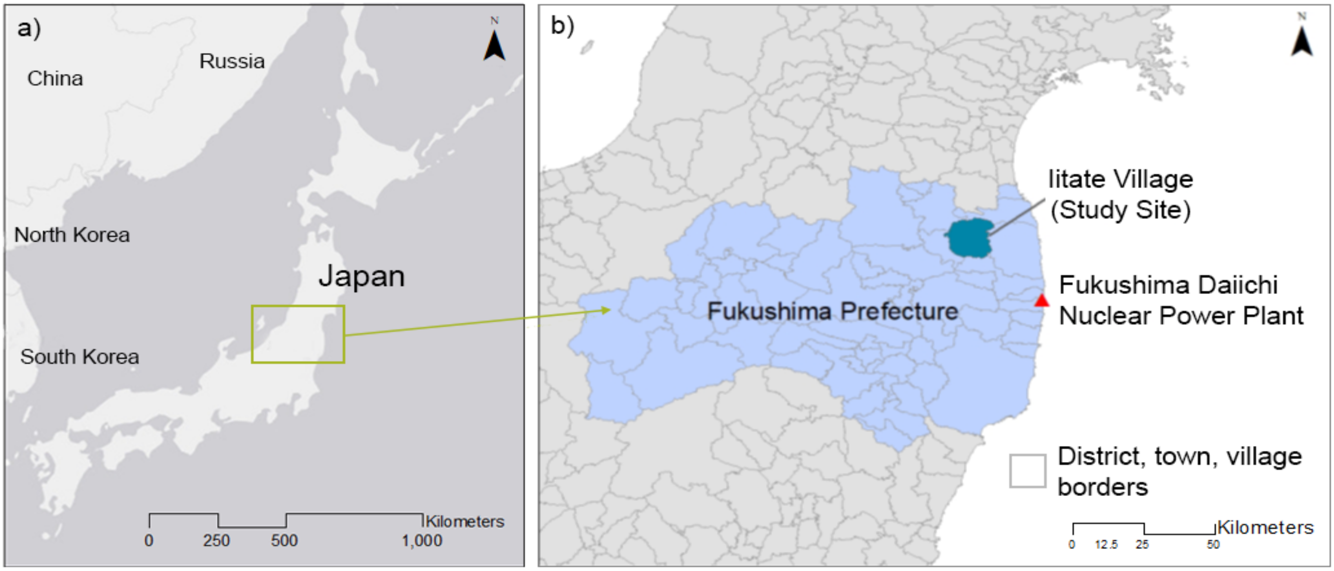

Fig. 1. Locations of the FDNPP and the study site (Basemaps: a) ESRI, HERE, Garmin, © OpenStreetMap contributors, and the GIS community; b) ESRI Japan).

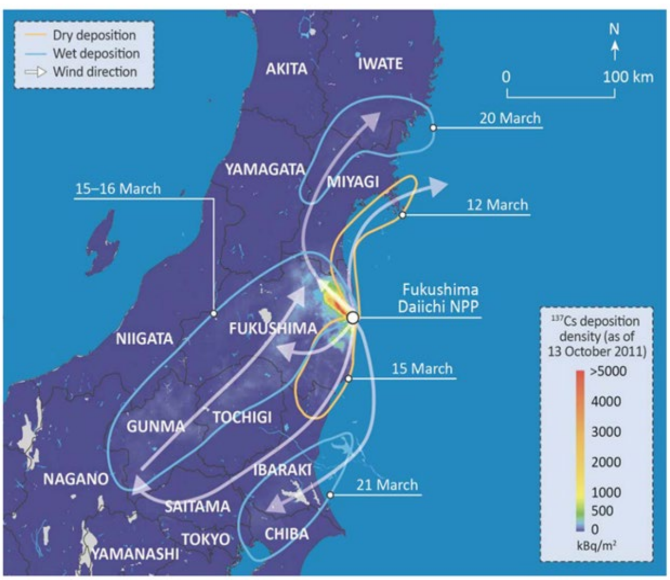

Fig. 2. Timing and locations of the main Cs-137 deposition events following the explosions at the FDNPP (Map: IAEA [2015]).

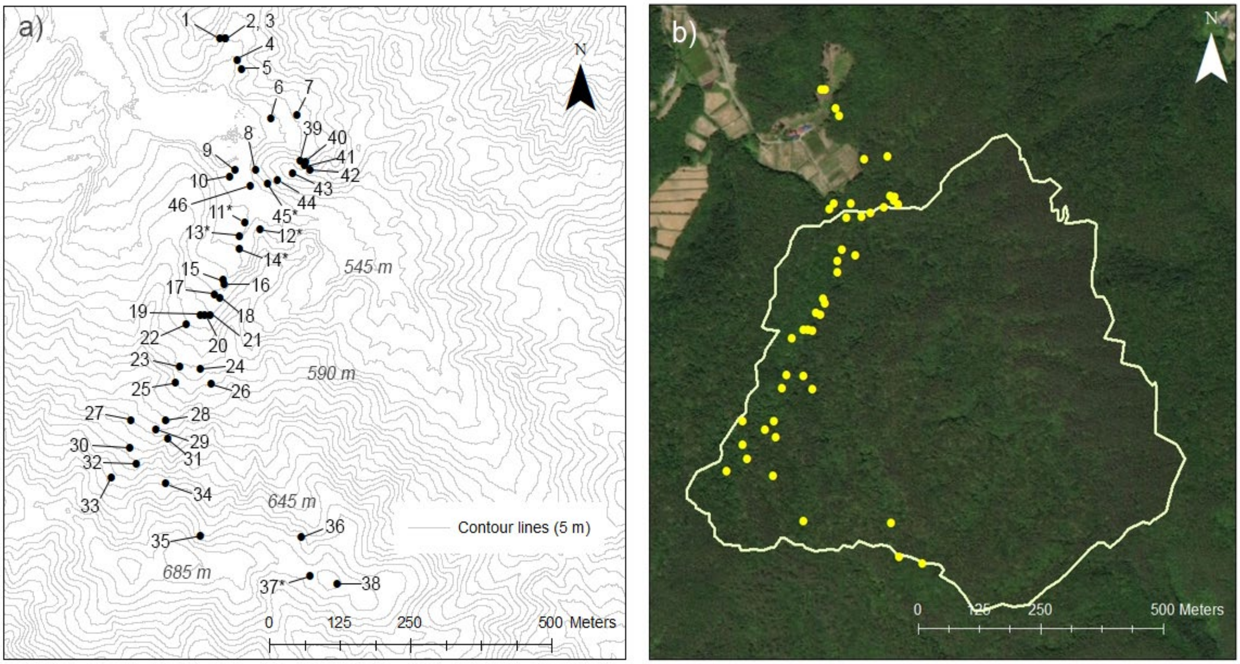

Fig. 3. Study site topography and aerial images. a) Numbered sample locations where multi-year samples were collected at the locations marked by * and contour lines are at 5-m intervals (Basemap: ESRI). b) A large basin enclosing the longest slope (Basemap: ESRI).

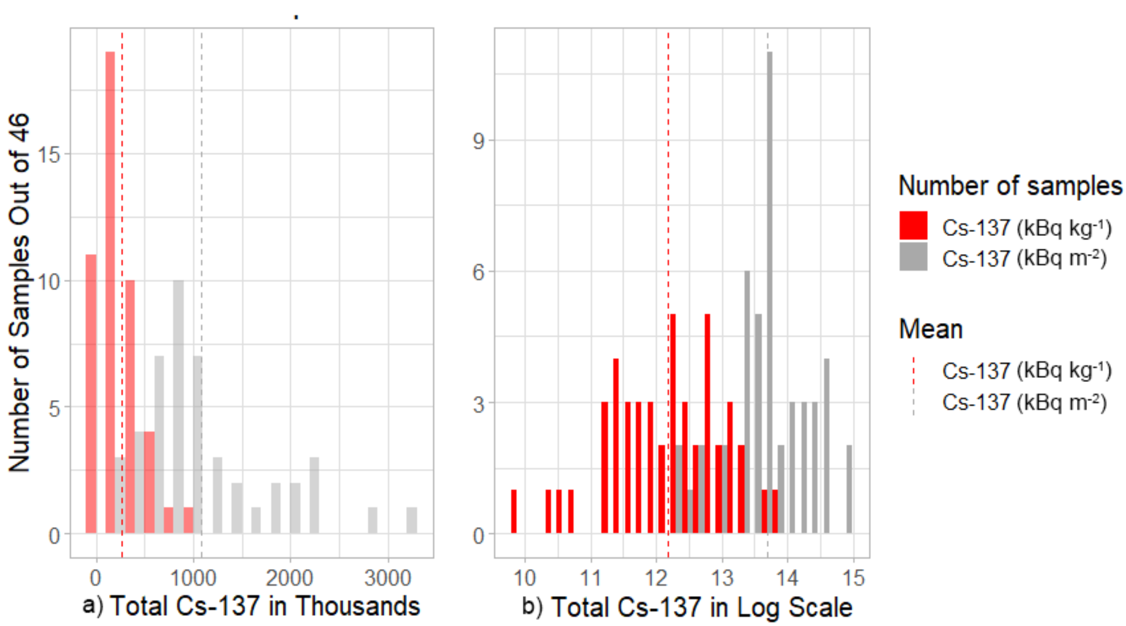

Fig. 4. Distribution of mass-based total Cs-137 in a core sample. (a) A unit of each bin is 200 k. (b) Distribution of total mass depth Cs-137 in a core sample in a log scale (red: Cs-137 kBq kg-1; grey: Cs-137 kBq m-2).

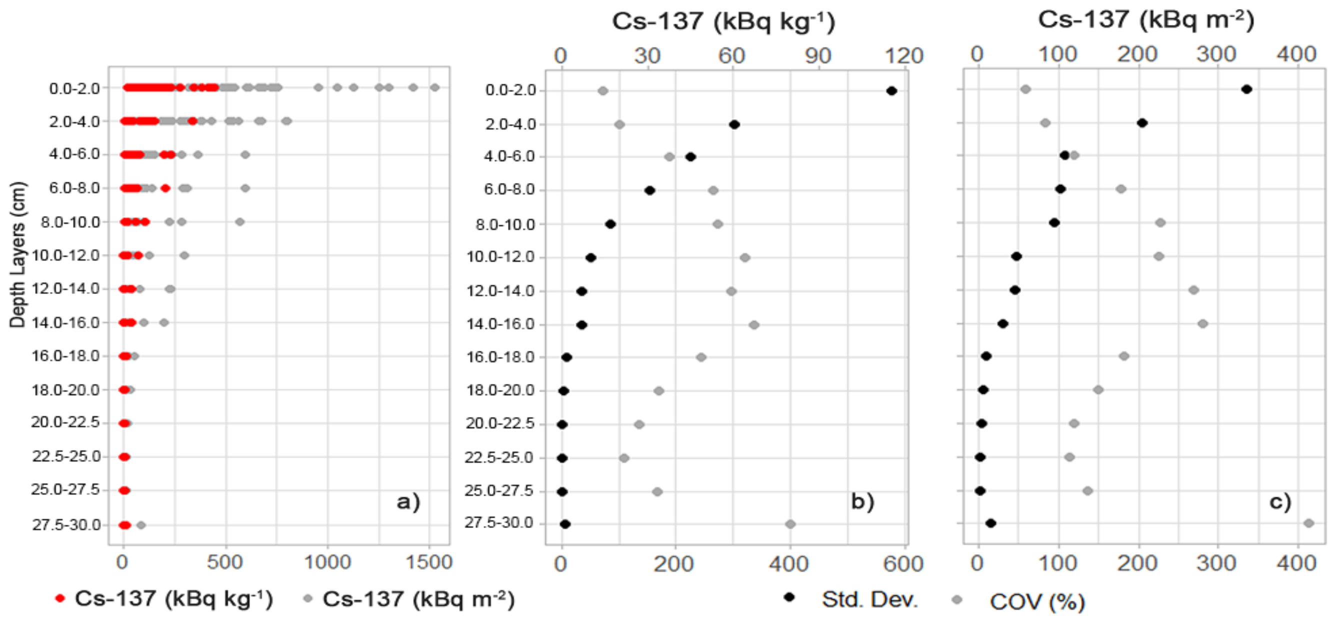

Fig. 5. (a) Depth distributions of Cs-137 concentrations in kBq kg-1 (red) and kBq m-2 (grey). Standard deviations (red) and COVs (grey) by depths in (b) kBq kg-1 and (c) kBq m-2.

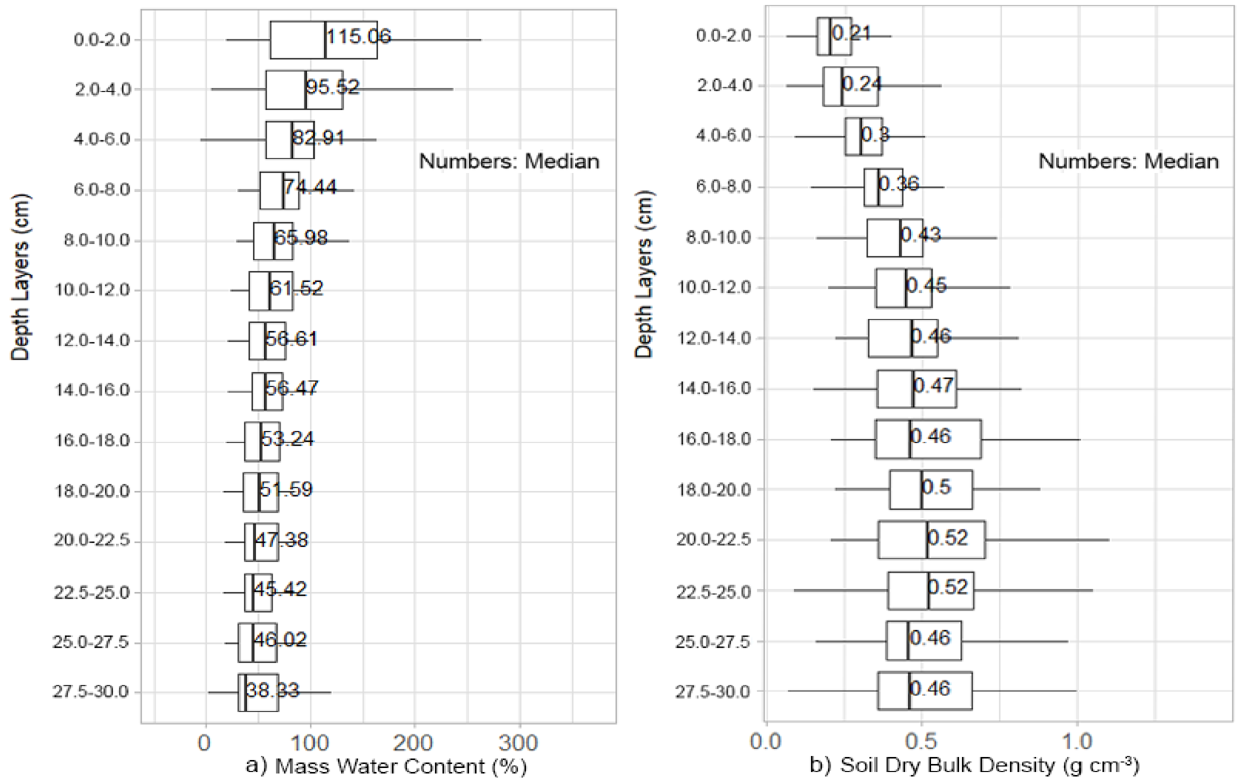

Fig. 6. Depth profiles of (a) mass water content (%) and (b) soil dry bulk density (g cm-3).

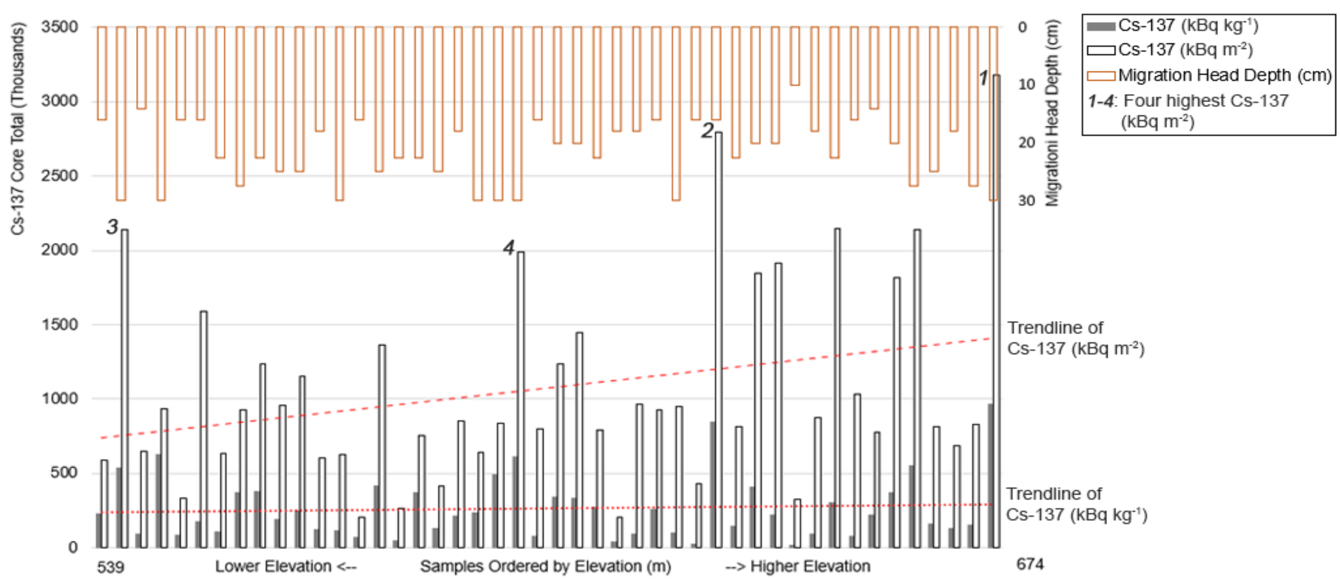

Fig. 7. Core total Cs-137 in both units along the elevation (m). Numbers 1-4 indicate the samples with the four highest Cs-137 concentrations in kBq m-2. Migration head depths (cm) are the depths at which Cs-137 concentrations decreased to 100 Bq kg-1 in a core sample.

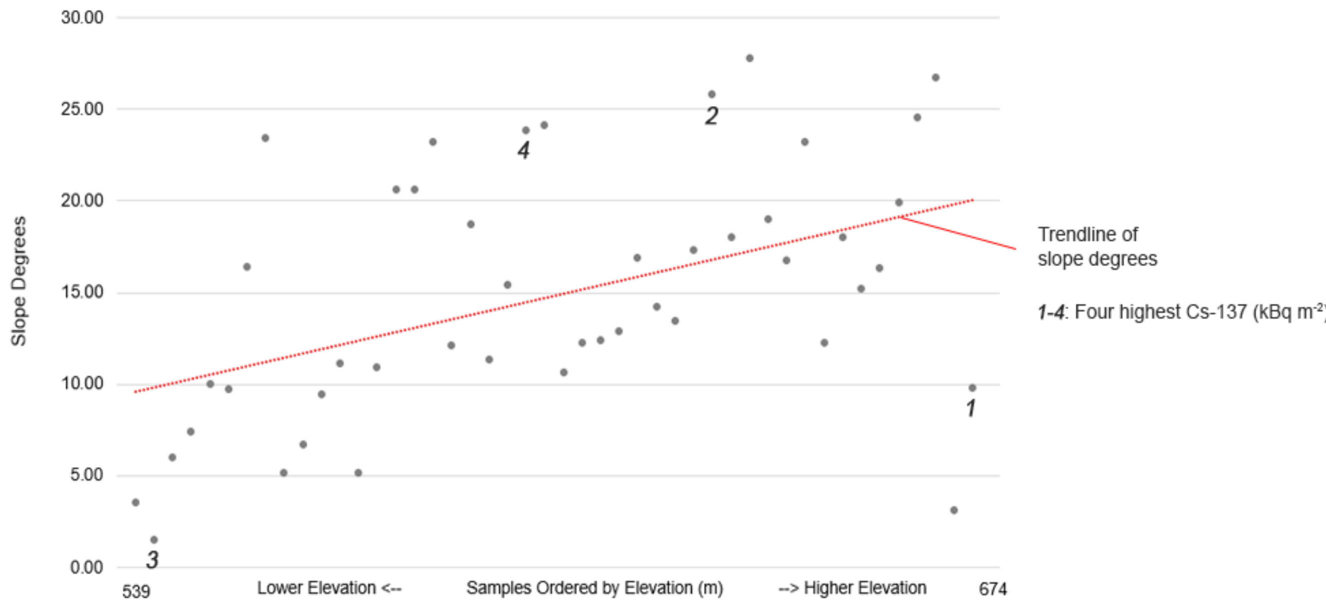

Fig. 8. Slope (degrees) of sampling points along the elevation (m). The numbers 1-4 correspond to the same numbers in Fig. 7.

875

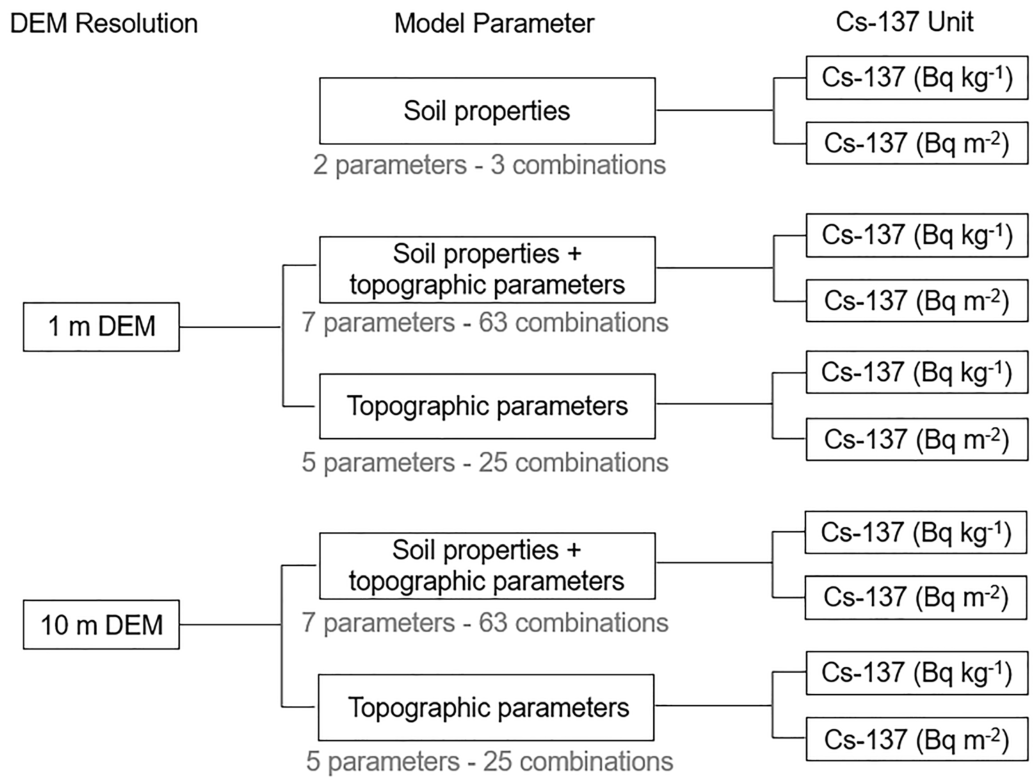

Fig. 9. GAM parameter combinations.

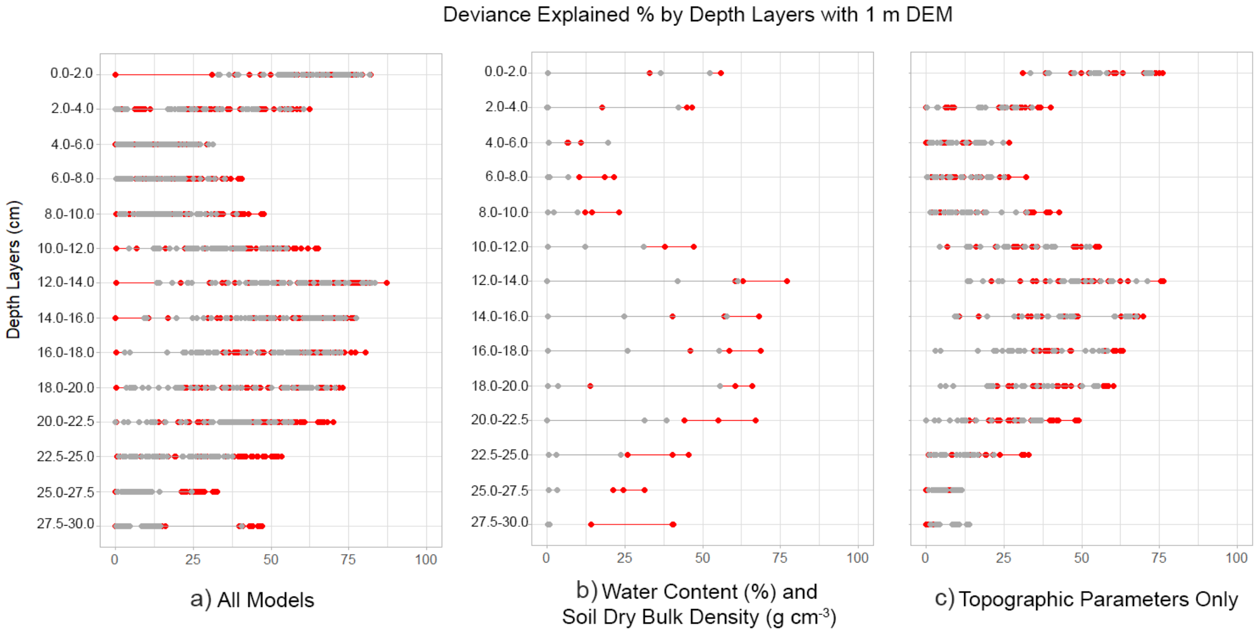

Fig. 10. Deviance explained percentages using the 1 m DEM. a) All parameter including combinations soil properties and topographic parameters. b) Parameter combinations with only water content (%) and soil dry bulk density (g cm-3). c) Parameter combinations with only topographic parameters.

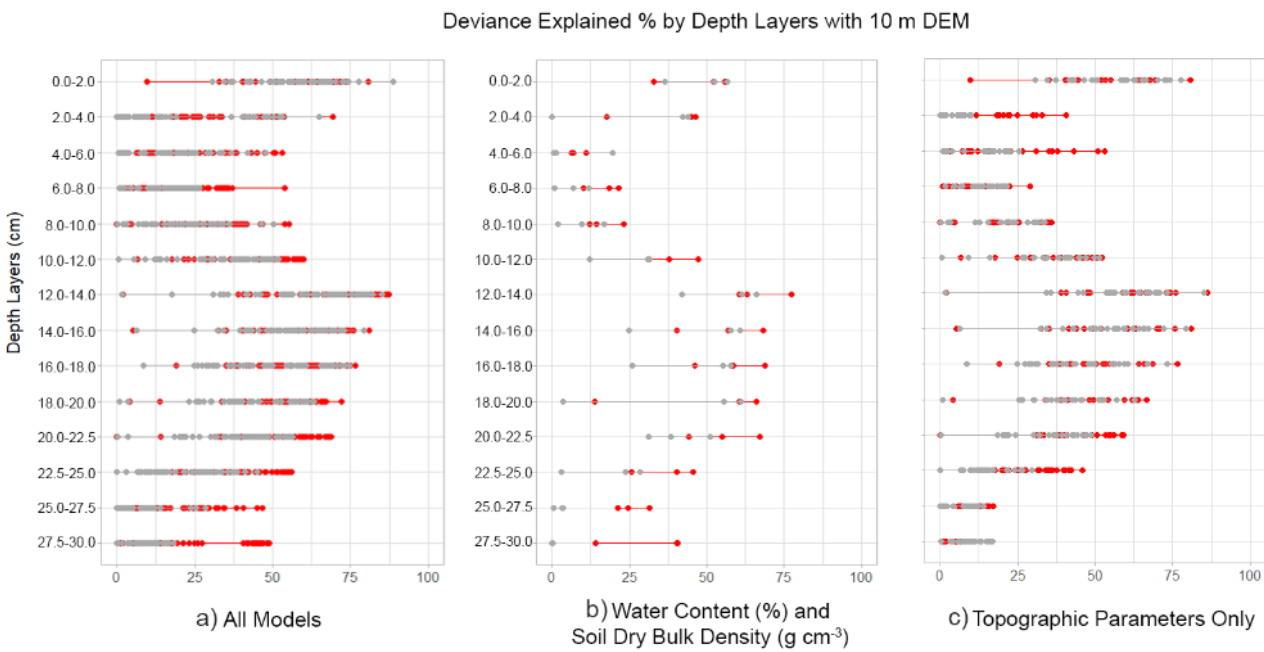

Fig. 11. Deviance explained percentages using the 10 m DEM. (a) All parameter combinations soil properties and topographic parameters. (b) Parameter combinations with only water content (%) and soil dry bulk density (g cm-3; the same graphic in Fig. 10 is repeated for the comparison purpose). (c) Parameter combinations with only topographic parameters.

Model A: Soil Properties and Topographic Parameters	**Model B: Topographic Parameters Only**
Water Content + Bulk Density + Elevation (Bq kg^{-1})	Elevation + Slope + Upslope Distance (Bq kg^{-1})

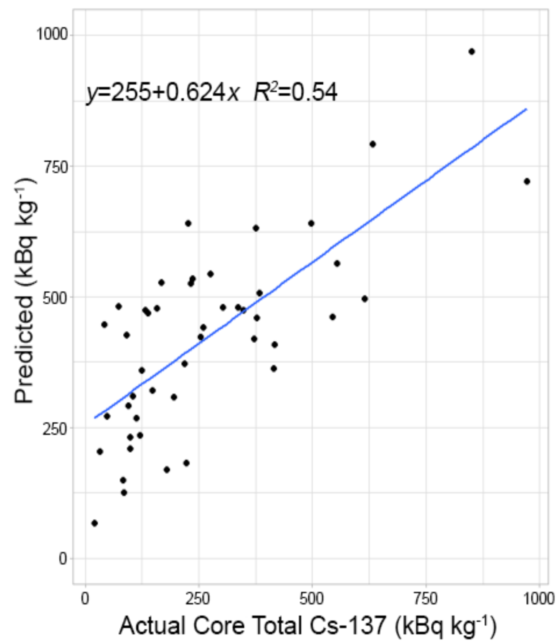

a) A scatter plot of the actual core total Cs-137 in and the predicted Cs-137, using Model A setting in Table 6.

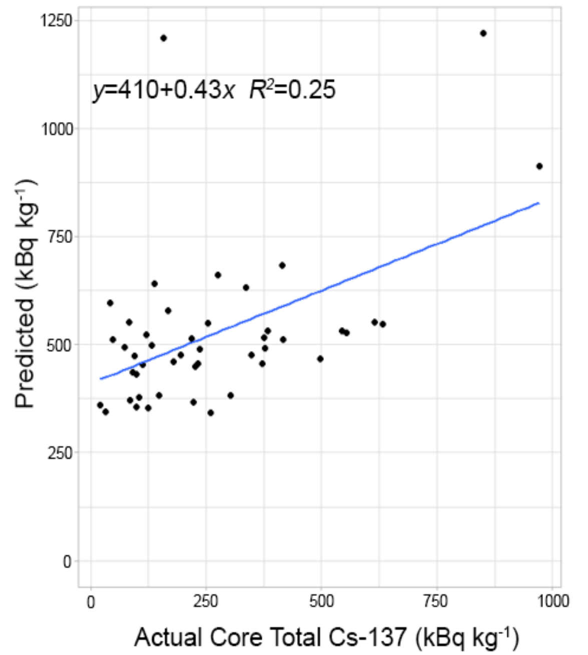

b) A scatter plot of the actual core total Cs-137 and the predicted Cs-137, using Model B setting in Table 6.

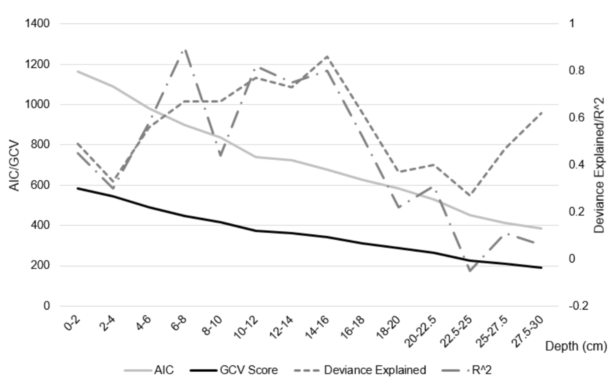

c) Model performance indices for Model A in Table 6.

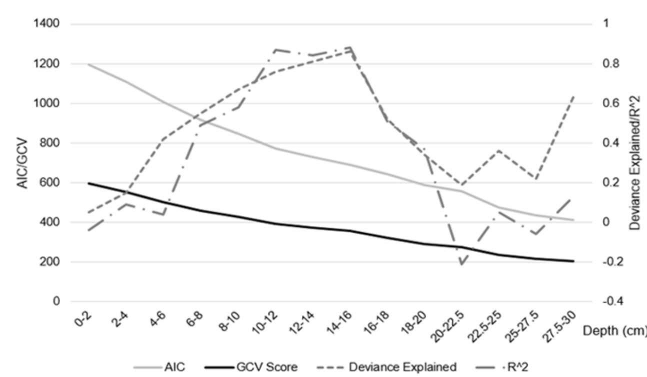

d) Model performance indices for Model B in Table 6.

Fig. 12. Top row: Regression analysis of actual and predicted Cs-137 activities. Bottom row: Model fit diagnosis results of the best-performing models (light grey: AIC; black: GCV score; dashed: deviance explained percentage: loosely dash-dotted: R2). Higher deviance explanation percentages and R2 values indicate how well the model explained, or approximate, the real data points. Lower AIC indicates a good model with less information loss (parsimony), and lower GCV suggests a good model with a smaller prediction error (Hastie, et al., 2009, Wood, 2017).

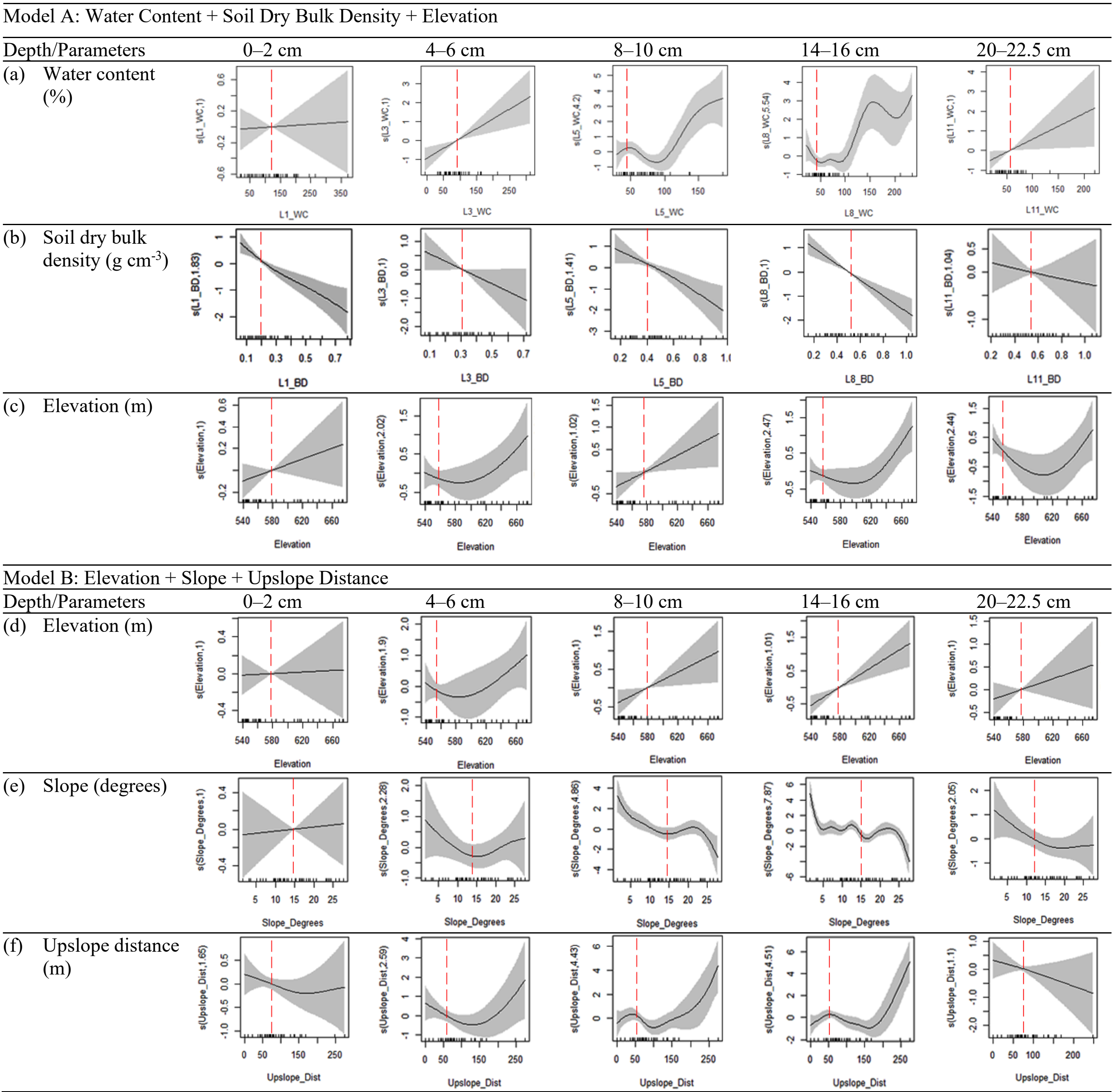

Fig. 13. GAM smooth function outputs at five depth layers for the parameters in the two best performing models. The x-axis on each plot is the model predictor and its real value range. The y-axis is the smoothing parameter, s(covariate, degree of freedom). Vertical red dashed lines indicate a point at which the smoothing parameter is the zero residual point.